PELLET INJECTION WITH IMPROVED CONFINEMENT IN ASDEX

M. Kaufmann, K. Büchl, G. Fussmann, O. Gehre,
K. Grassie, O. Gruber, G. Haas, G. Janeschitz,
M. Kornherr, K. Lackner, R.S. Lang, K.F. Mast,
K. McCormick, V. Mertens, J. Neuhauser, H. Niedermeyer,
Z.A. Pietrzyk*, W. Sandmann, D. Zasche, H.P. Zehrfeld

IPP 1/242 July 1987

MAX-PLANCK-INSTITUT FÜR PLASMAPHYSIK
8046 GARCHING BEI MÜNCHEN

MAX-PLANCK-INSTITUT FÜR PLASMAPHYSIK

GARCHING BEI MÜNCHEN

PELLET INJECTION WITH IMPROVED CONFINEMENT IN ASDEX

M. Kaufmann, K. Büchl, G. Fussmann, O. Gehre,
K. Grassie, O. Gruber, G. Haas, G. Janeschitz,
M. Kornherr, K. Lackner, R.S. Lang, K.F. Mast,
K. McCormick, V. Mertens, J. Neuhauser, H. Niedermeyer,
Z.A. Pietrzyk*, W. Sandmann, D. Zasche, H.P. Zehrfeld

IPP 1/242 July 1987

* University of Washington, Seattle, Wash. 98195, USA

Die nachstehende Arbeit wurde im Rahmen des Vertrages zwischen dem Max-Planck-Institut für Plasmaphysik und der Europäischen Atomgemeinschaft über die Zusammenarbeit auf dem Gebiete der Plasmaphysik durchgeführt.

PELLET INJECTION WITH IMPROVED CONFINEMENT IN ASDEX

M. Kaufmann, K. Büchl, G. Fussmann, O. Gehre,
K. Grassie, O. Gruber, G. Haas, G. Janeschitz,
M. Kornherr, K. Lackner, R.S. Lang, K.F. Mast,
K. McCormick, V. Mertens, J. Neuhauser, H. Niedermeyer,
Z.A. Pietrzyk*, W. Sandmann, D. Zasche, H.P. Zehrfeld

IPP 1/242

* Z.A. Pietrzyk, University of Washington, Seattle, Wash. 98195, USA

Abstract

Tokamak discharges with repetitive pellet fueling were investigated in the ASDEX divertor device. The importance of sufficiently high divertor recycling for successful density build-up in the bulk plasma was demonstrated. In OH-heated discharges with high recycling an energy confinement time of 160 ms was reached, the normal values being 80 ms in the roll-over region. The peaked density profiles in this cases were accompanied by reduced or suppressed sawtooth activity and finally ended in a phase of strong central impurity accumulation. The particle transport was characterized by strong, non-classical inward drift, while the improved energy transport can be explained by two alternatives: (1) a local model which assumes neo-Alcator χ_e for the electrons and an $\chi_i = 3\chi_{neocl}$ for the ions in the gas puff cases reduced to $\chi_i = \chi_{neocl}$ for the optimum pellet cases; (2) a profile consistency picture were $T_e(a)$ determines the energy confinement. Low-power, NI-heated discharges with pellet fueling behave like ohmic discharges, while for high power in the L-mode no successful density build-up was possible, and τ_E was not improved. The H-regime was extended to $\bar{n}_e = 1.2 \cdot 10^{20} m^{-3}$ by the injection of pellets. In this case a density build-up takes place, but a further density profile peaking could not be observed.

Pellet Injection with Improved Confinement in ASDEX

M. Kaufmann, K. Büchl, G. Fussmann, O. Gehre, K. Grassie, O. Gruber, G. Haas, G. Janeschitz, M. Kornherr, K. Lackner, R.S. Lang, K.F. Mast, K. McCormick, V. Mertens, J. Neuhauser, H. Niedermeyer, W. Sandmann, W. Schneider, D. Zasche, H.P. Zehrfeld, Max-Planck-Institut für Plasmaphysik, EURATOM Association, D-8046 Garching,
Federal Republic of Germany

Z.A. Pietrzyk, University of Washington, Seattle, Wash. 98195,
United States of America

1. Introduction

Injection of frozen hydrogen pellets was proposed and developed as a method for deep fuelling of fusion devices. In addition, pellet injection turned out to be an interesting tool for plasma diagnostics, and, under certain circumstances, there is substantial improvement of energy and particle confinement of the plasma [1,2]. This improvement sometimes observed raises the questions: what is the prerequisite for it, what changes to the plasma does it entail, and, finally, what is the physical explanation for it?

This paper presents results obtained in ASDEX with a centrifuge injector [3] which clearly show the improvement of energy and particle confinement compared with gas-fuelled discharges. These discharges are also compared with results of pellet-fuelled discharges where no improvement was observed [4], and the differences are discussed. Clean plasma conditions achieved by operation with the divertor and partly by carbonized walls [5] and combination with gas puffing led to long-lasting, well observable periods of good confinement. In addition, some specific diagnostics at the plasma boundary enabled us to correlate the bulk plasma behaviour and the properties at the plasma edge and to narrow down a possible explanation of the improved confinement substantially.

The ASDEX plasma parameters of the discharges discussed here and the data of the centrifuge system are presented in Sec. 2. The essential phenomenological properties of the two cases, with improved and with "normal" confinement, and their dependence on recycling are then contrasted in Sec. 3. The improvement of particle transport in the bulk plasma as the typical hallmark of good confinement and its dependence on the sawtooth activity are demonstrated in Sec. 4. Specific results were obtained with slow pellets and shallow penetration (Sec. 5). In Sec. 6 phenomena occurring in the late phase of a good-confinement discharge, where impurity accumulation governs the discharge, are discussed. It is found that this late phase and its physical properties can be clearly separated from the phase where the change to good confinement happens. Information from plasma boundary measurements and their correlation to the bulk plasma behaviour are given in Sec. 7. The influence of pellet injection into plasmas with additional heating is described in Sec. 8. finally (Sec. 9), the possible physical interpretation of plasma edge behaviour and bulk plasma confinement are discussed. The conclusions (Sec. 10) deal with the potential of pellet injection to improve the plasma performance.

2. Operation Parameters

The ASDEX device was run at, typically, $B_t = 2.17\ T$ with a current of $I_p = 380\ kA$, corresponding to a cylindrical safety factor of $q_c = 2.7$ $\left(q_c \equiv \frac{2\pi \cdot B_t \cdot a^2}{\mu_o \cdot I_p R}\right)$. Besides these standard values, discharges with $B_t = 2.36\ T$, $I_p = 320$ to $380\ kA$, $q_c = 2.77$ to 3.57 were also investigated. The double-null divertor was used throughout this campaign and in typical cases of good confinement the machine was carbonized. It was also possible, however, to observe the essentials of good confinement without carbonization. The density range extended from $\bar{n}_e = 0.2 \times 10^{20}\,\mathrm{m}^{-3}$ to $\bar{n}_e = 1.2 \times 10^{20}\mathrm{m}^{-3}$, while in the earlier investigation [4] $\bar{n}_e$ was as low as $0.1{\times}10^{20}\mathrm{m}^{-3}$ before pellet injection. The standard filling gas was deuterium. The investigation concentrated on cases with ohmic heating, but discharges with additional heating by co and counter neutral injection together with pellet injection are considered as well.

The standard centrifuge [3] range was 1 to 80 pellets with about 4×10^{19} deuterium atoms each, with a velocity of 620 m/s. Typical values for pellet injection were 5 to 20 pellets. The interval between pellets was typically 30 ms, ranging from 20 to 100 ms. The penetration depth was about half the plasma radius (15 to 25 cm) for ohmic discharges, while in plasmas with additional heating the penetration depth was reduced to 10 to 20 cm. In a limited series of discharges pellets with a velocity of only 200 m/s were used, penetrating up to 7 cm deep. The pellets were monitored with a microwave mass detector [6], with an $H\alpha$ detector and partly by photographic observation.

3. Phenomenology of "Normal" and Improved Confinement Discharges

Discharges with the centrifuge pellet injector in ASDEX were performed in a first campaign to demonstrate the potential of very low recycling at the plasma boundary by combining divertor operation and pellet fuelling. In a second campaign the investigation was aimed at reaching high plasma densities even at the expense of high recycling. Typical low-recycling pellet (LRP) discharges dispensed with gas puff parallel to the injection, and the pellet injection started early in the discharge at typically $\bar{n}_e = 0.1\times10^{20}m^{-3}$. In the high-recycling pellet (HRP) discharges, pellet injection started typically later in the discharges at higher densities and mostly used gas puff in addition to pellet fuelling. In the following, discharges with gas-puff fuelling only are referred to as "GP".

As a first approach LRP and HRP discharges can be identified by looking at the trace of the interferometric signal [7]. Figure 1 contrasts different cases where the averaged plasma density is determined from the horizontal channel through the midplane. The HRP discharge (Fig. 1b) shows a much more successful density build-up than the LRP discharge (Fig. 1a). A more quantitative comparison can be introduced by defining a fuelling efficiency η_f, which is the ratio of the total change in plasma ions ΔN_t to the number of injected pellet deuterons ΔN_p counted for and averaged over a certain time Δt:

$$\eta_f = \overline{\left(\frac{\Delta N_t}{\Delta N_p}\right)}^{\Delta t} .$$

Although there is some arbitrariness in the selection of Δt, η_f turns out to be a much better working-horse to describe changes in particle confinement than the global particle confinement time. The total particle content of the plasma was determined by Thomson scattering with a 16-channel YAG laser system with a frequency of 60 Hz [8] which was calibrated early in the discharge by the interferometer. The particle content of each pellet was measured with a microwave cavity [6].

In the HRP discharge of Fig. 1b the fuelling efficiency thus determined for the time period $t = 1.4s$ to $t = 1.7s$ is $\eta_f = 0.50$, while in the LRP discharge of Fig. 1a for $t = 0.5s$ to $t = 1.0s$ the efficiency is as low as $\eta_f = 0.10$, Δt being chosen as 100 ms, averaged over several pellets.

In a discharge with variable gas puff during pellet injection (see Fig. 1c) it can be observed that, with some delay, the fuelling efficiency follows the gas puff and can reach unity under optimal conditions. In this case η_f was determined by averaging over the pellet cycle.

Density and temperature profiles for several points in time are already shown in [9] for shot #18710, which is very similar to shot #18716 (Fig. 1b). The development of the central density and temperature and of profile factors of a typical HRP discharge can be seen in Fig. 2a. The density during pellet injection essentially changes by rising and peaking in the centre. It remains peaked even when the pellets are switched off for a time of about 230 ms. Even small further peaking and inward drift from about half the radius to the centre can be observed in this phase. The temperature profile drops somewhat during pellet injection but remains nearly self-similar up to the end of pellet injection or the end of the stationary post-pellet phase.

The improvement of the energy confinement time τ_E averaged over a pellet cycle for HRP discharges is clearly seen in Fig. 2b ($\tau_E \equiv \frac{1.9\times W_e}{P_{OH}-1.9W_e}$; W_e: energy content of electrons from Thomson scattering data; P_{OH}: ohmic heating power; no correction for radiation; the assumption that the ions have 90% of the energy content of the electrons is conservative at these high densities.) The parallel developments of the electron energy content W_e and particle content N_e can readily be seen. Values of the energy confinement time τ_E calculated from diamagnetic data show an increase by pellet injection of about 20% less compared with τ_E calculated from the kinetic data. From the vertical magnetic field together with an equilibrium calculation, and a determination of l_i one gets τ_E values typically 20% higher in total, but again with a smaller relative increase.

The energy confinement time τ_E as a function of the line-averaged density $\bar{n}_e$ is compared for three different cases (see Fig. 3): standard ohmically heated ASDEX discharges with gas puff only (GP) and pellet injection with low recycling (LRP) and with high recycling (HRP). The deterioration of τ_E in LRP discharges compared with GP discharges can be attributed to convection and radiation, as discussed in [4]. The local parameters describing energy and particle transport in these cases are not substantially changed by pellet injection. In contrast, there is a substantial improvement of confinement from GP to HRP discharges. If we exclude the late phase with strong central radiation, we get the following picture: The temperature profile nearly keeps its relative shape and the amplitude is only somewhat reduced, parallel to a reduction of Z_{eff} [10]. The heating power thus drops to its original value after a transient phase. At the same time the particle transport changes as a consequence of pellet injection. Reduced diffusion and/or increased inward drift lead to peaking of the density profile. The increased particle content together with about the same heating power and temperature profile results in the increased energy confinement time.

The improvement in energy confinement by means of pellets just for those density values where the normal GP data show a saturation of τ_E with $\bar{n}_e$ may suggest that the pellets restore the situation in the linear part of the $\tau_E/\bar{n}_e$ curve and remove the reason for the roll-over. A detailed discussion of this question will follow in Sec. 9. But it can be pointed out already in the course of the description of the phenomenology that the peaked density profile in HRP discharges seems to establish a new type of discharge. The density profiles with GP for different $\bar{n}_e$ values - in the linear and the saturated regimes - are nearly self-similar (q = const) [11], whereas n_e profiles with pellets are substantially more peaked. The improved energy confinement with slow pellets at low density (see Sec. 5) has also to be observed in this context.

In the HRP discharges with improved particle confinement it was possible to increase the density limit [12,13]. A value of $\bar{n}_e = 1.10 \times 10^{20}\,\mathrm{m}^{-3}$ for the averaged density, which corresponds to a Murakami parameter of $8.4 \times 10^{19}\,\mathrm{m}^{-2}\,\mathrm{T}^{-1}$, and a central density of $n_e(0) = 2.45 \times 10^{20}\,\mathrm{m}^{-3}$ were reached. The corresponding data from GP discharges on the same day were $\bar{n}_e = 0.63 \times 10^{20}\,\mathrm{m}^{-3}$ and $n_e(0) = 0.80 \times 10^{20}\,\mathrm{m}^{-3}$. The plasma behaviour close to the density limit in the late disruption phase could be well separated from the earlier phase of pellet injection, where improved particle and energy confinement was observed. For a more detailed analysis see Sec. 6.

The MHD activity was monitored by a soft X-ray detection system and by Mirnov coils. Usually no specific MHD activity could be observed during pellet injection in OH-discharges. The sawteeth, typically without pronounced precursor, remained unchanged in sequence and amplitude during the first few pellet cycles. In an HRP discharge the sawtooth activity changed later on and finally disappeared (see Secs. 4 and 9 for further details and discussion). The soft X-ray system showed strong poloidal asymmetries in the first few milliseconds after each pellet injection with an m=1 like structure [14]. Strong MHD activity detected by magnetic pick-up loops can be found late in the discharge at a high central radiation level (see Sec. 6b). Further pronounced and specific MHD activity is correlated to strong neutral injection heating and is described in Sec. 8.

In a separate campaign q_c was varied between 2.8 and 3.6. Five pellets were injected into each of these discharges. Because of the limited number of pellets and the limited injection time no final stationary phase could be obtained. However, in all discharges it was possible to observe clearly peaking of the density profile and an increase of the energy confinement time. In addition, we observed a tendency to stronger increase of the total particle content and stronger peaking at higher q_c-values.

4. Bulk Plasma Particle Confinement

Improved energy confinement with pellet injection was correlated in all ASDEX discharges to successful density build-up. This build-up calls for the appropriate behaviour of the plasma boundary and proceeds parallel to distinct changes in the bulk plasma particle transport. This section is concentrated on a discussion of the changes in the bulk plasma, while a description of the plasma edge behaviour will follow in Sec. 7. Throughout this section we concentrate on those cases of proper edge conditioning where the fuelling factor η_f (see Sec. 3) is relatively high ($\eta_f \gtrsim 0.5$).

The observed peaking of the central density profile cannot be attributed to central deposition of particles by the pellet injection. In the typical HRP discharge the density rises in the centre although the penetration depth of the pellets is between 20 cm and 25 cm only, and the peaking remains up to 230 ms after the last pellet.

Hence the experiments clearly show a change of the particle transport during and after pellet injection. Apart from exceptions, the pellets did not reach the q=1 radius ($r_{q=1} \lesssim 10\,\mathrm{cm}$).

We describe the radial particle transport in a simulation by the following ansatz:

$$\frac{\partial n_e}{\partial t} - S_e(r,t) = -\nabla\Gamma_e = -\frac{1}{r}\frac{\partial}{\partial r}(r \cdot \Gamma_e), \tag{1a}$$

$$\Gamma_e \equiv n_e v_r(r) = D(r) \cdot n'_e - v_{in}(r) \cdot n_e \tag{1b}$$

($S_e(r,t)$: particle source per unit time and volume, D: particle diffusion coefficient, v_{in}: inward drift velocity, $n'_e = \frac{\partial n_e}{\partial r}$). The necessity of describing transport by an inward drift in addition to the diffusion term proportional to n'_e has already been pointed out on several occasions [e.g. 15]. The ratio between D and v_{in} can easily be derived for nearly stationary and source-free profiles ($\Gamma_e \approx 0$): $v_{in}/D = n'_e/n_e$ This is applicable as a good approximation to the situation before pellet ablation and to the stationary phase afterwards for $r \lesssim 35$ cm. Figure 4 compares $v_{in}/D = n'_e/n_e$ before (Fig. 4a) and after (Fig. 4b) pellet injection; $n_e(r)$ is shown as a dotted curve in both cases. Especially in the inner two-thirds of the radius v_{in}/D has increased by a factor of 3 or more, demonstrating the change in particle transport.

To tackle the dynamics of this change during pellet injection, one has to analyze a sequence of $n_e(r)$ profiles. This analysis is limited by the imperfection of the diagnostic system. On the one hand, interferometric signals often fail during pellet injection with peaked profiles because of miscounting of fringes and beam deflection, especially at the half-radius. On the other hand, the YAG laser system provides data every 17 ms only. The effect of a particle source provided by the ablated pellet therefore cannot easily be separated from profile development by inward drift and diffusion by investigating the interval between two pellets only. To get limited information, we proceed as follows: the total particle number of each pellet was determined by the mass detector. The radial dependence of the particle deposition was set proportional to the H_α signal [16]. Both the radial distribution of the particle source $S_e(r)$ and the measured density profile were smeared out in time by averaging over a time interval ± 17 ms. Figure 5a shows the density profile development $n_e(r,t)$. The corresponding net particle flux $\Gamma_e(r,t)$, which is necessary to describe the observed changes in n_e, taking into account the source term $S_e(r,t)$, is given in Fig. 5b for typical time periods before and during the build-up phase. One can clearly identify a net inward motion of particles from the region where most of the pellet mass was ablated to the centre. The outward flux in the outer region describes that fraction of the pellet mass which is lost. The inward motion starts more or less with the first pellets and continues during injection. Before and after injection particle fluxes are small.

To describe the particle flux by a diffusion coefficient and an inward drift according to eq. (1), we tried to determine D and v_{in} separately during the density build-up by a fit to the following expressions:

$$D = D_o \qquad v_{in} = r/a^{\alpha} \cdot v_{in}(a).$$

It was possible to fit the observed flux Γ_e by
$D_o = 0.1 \pm 0.05 m^2/s, \qquad \alpha \approx 1, \qquad v_{in}(a) = 1.0 \pm 0.2 m/s.$

It has to be pointed out that these parameters are only of limited value: there is a certain arbitrariness in the ansatz for D and v_{in} and on the basis of the existing experimental data one cannot prove that the selected expression and the fit parameters are unique in describing the transport. However, this method yields the order of magnitude of the velocity of generally observed inward drift.

The peaking of the density profile and the increase of v_{in}/D in the central part of the discharge is always correlated to a reduction of the sawtooth activity. The regular sawteeth before pellet injection go through an irreproducible intermediate phase, where they get less frequent and often lock to the pellet period: one sawtooth appears at a certain time after injection. In the final stationary phase after pellet injection the sawtooth activity completely vanishes. A calculation of the current profile from the temperature and density profiles shows in parallel a small but significant increase of q on axis (because of the long time scale the skin effect was neglected). $q(0)_{neoc}$ increases typically from 0.85 to 1.0 during pellet injection in a discharge with successful density build-up compared with the pre-pellet phase. This increase clearly happens before impurity accumulation, strong central radiation and a further temperature flattening in the centre late in the discharge.

5. Injection of Slow Pellets

A limited series of discharges was carried out with relatively slow pellets of 200 m/s only. Up to three pellets were injected into an ohmically heated plasma ($B_t = 2.3T, I_p = 300kA$, starting density $\bar{n}_e = 1.3 \times 10^{19} m^{-3}$) after neutral injection or lower hybrid heating. Although the injection took place 110 – 130 ms after the lower hybrid heating, a remaining population of non-thermal electrons seemed to persist. An analysis of the ECE spectra yields a value of about 1% non-thermal electrons immediately after lower hybrid heating, decaying with a time constant of 75 ms. As a consequence and detectable by photographic observation, and the H_α-signal part of the pellet was ablated by non-thermal electrons close to the separatrix [17]. Besides this effect, penetration of up to 7 cm (typically 5 cm) was observed for these slow pellets.

Despite the shallow penetration an inward drift of the ablated material can readily be observed. Figure 6a shows $n_e(r,t)$ for such a case with three pellets. The ablated material moves inward with $v_{in} \approx 0.3m/s$ (at r=0.4 a). The relative density profile broadens after each pellet and peaks afterwards, reaching a final value of $n_e(0)/\bar{n}_e$ about 10% higher than before. There was no sawtooth activity during the injection phase. The experiment terminated at the preprogrammed end of the current pulse. It was therefore not possible to detect a stationary phase with a peaked density profile.

The energy confinement time τ_E during this non-stationary phase of injection continuously rose, starting from 60 ms, to a value of around 100 ms (see Fig. 6b) and was clearly above the standard GP values in the linear part of the $\tau_E(\bar{n}_e)$ curve. This τ_E increase cannot be attributed to heating by the non-thermal electrons. Their heating power was estimated to be 5% or less compared with ohmic heating.

Summarizing the slow pellet results, one gets the impression that they show the typical HRP signature despite the shallow penetration, but final proof was not possible because of experimental limitations in this campaign.

6. Impurity Behaviour and the Late Phase of HRP Discharges

6a. The central impurity accumulation

In typical HRP discharges (divertor operation, carbonized wall) pellets were injected into relatively clean plasmas with Z_{eff} (neocl.) usually between 1.2 and 1.5, and with a total radiation loss P_{rad}/P_{total} of 20 – 25% measured by bolometers. During the density build-up, and in the stationary phase after injection, Z_{eff} (neocl.) dropped less than 0.2 while the total radiation loss went up to typically 30 – 50%. In contrast to the moderate increase of total radiation the central radiation finally increased drastically up to a level locally equal to the heating power. This happened in all cases with a peaked density profile. The increase of central radiation was usually delayed to the increase of the central density, and no saturation at any level was observed. The increase was also independent of whether pellet injection continued or whether a stationary peaked phase without injection was obtained. Finally, around the radiation level $P_{rad}(0)/P_{OH}(0) \approx 1$ or higher, one or a sequence of internal disruptions followed, leading to a discharge with strongly reduced energy and particle content. Figure 7 compares the time evolution of the radial dependence of the radiation loss in a GP discharge (Fig. 7b) with that in an HRP discharge (Fig. 7a); both discharges run into their specific density limit. While at this q value of 2.7 the GP discharge terminates with strong boundary radiation and marfes, the HRP discharge reaches its density limit (see end of Sec. 3) through strong central radiation and a specific internal disruption.

The soft-X-ray radiation peaks together with the bolometric signal. An analysis of spectral lines clearly showed peaking and a strong central increase of high-Z material such as titanium and iron. The strong increase starts approximately with the disappearance of the sawtooth activity and rises exponentially with a time constant of about 100 ms up to the internal disruption [18]. Typical central concentrations of $2 \times 10^{-4}\%$ for Fe and $4 - 8 \times 10^{-3}\%$ for Ti were reached. $FeXVI$-line radiation originating from the outer plasma region ($r \approx 33$ cm) showed no increase parallel to the central increase, indicating an unchanged total Fe confinement time and unchanged Fe sources. Charge-exchange resonant-scattering measurements showed, furthermore, that low-Z material such as oxygen and carbon did not strongly accumulate.

An attempt to simulate the observed strong accumulation of titanium was made. As outlined in [19], the impurity fluxes are composed of three terms: $\Gamma_Z(r,t) = \Gamma_s(r,t) + \Gamma_{an}(r) + \Gamma_{neoc}(r,Z)$, describing, respectively, the pulse-like impurity expulsion caused by the sawteeth, the anomalous diffusion and inward drift needed to describe the background plasma, and the neoclassical impurity transport. In order to allow strong central peaking of titanium due to the neoclassical inward drift, the anomalous diffusion coefficient must be kept rather low $D_{an} \leq 0.04m^2/s$. The combined anomalous and neoclassical terms are of the order $0.05 \leq D \leq 0.07m^2/s$ and $a \leq v_{in} \leq 5m/s$, both attaining their maximum at the plasma boundary. Figure 8a shows a computed 3D titanium profile for a case where four pellets were injected into an NI-heated discharge (0.9 MW counter NI, carbonized conditions). In the calculation all observed sawteeth were explicitly taken into account as described in [19] with equal amplitude. The figure clearly demonstrates that accumulation is prevented as long the repitition time is sufficiently short. The comparison with measured Ti XX and soft x-ray intensities is depicted in Fig. 8b.

6b.The internal disruption at high central radiation

After the description of the late phase with its strong central radiation and high-Z accumulation, we shall try to correlate the final disruption of the plasma to a violation of the ballooning criterion. This phase is characterized by a very peaked pressure profile coinciding with a relatively flat temperature profile. One should therefore expect a tendency to become ballooning-unstable in the centre. For quantitative analysis the data were analyzed in the following way: The pressure profile was expanded around the magnetic axis by $p(r) = p_0 - p_2 \times r^2$ and the current profile by $j(r) = j_0(1 - j_2^* \times r^2)$. The value of p_2 was fitted to the YAG n_e and T_e data in the inner third of the plasma. From the same data j_2^* was determined by assuming Spitzer's resistivity, by neglecting the inductive effect (this is a good assumption because of the stationary state), and by assuming Z_{eff} to be constant over the radius [10]. Neoclassical conductivity increases p_2^{crit} in the late phase after pellet injection by only about 20%. The current profile determines a critical pressure p_2^{crit} [20] by

$$p_2^{crit} = \frac{0.88 \cdot j_2^{*1/2} B_t(R)^2}{4\mu_0 q(0)^2 R}.$$

In Fig. 9 we compare p_2^{exp} and p_2^{crit} as functions of time for a typical HRP discharge with a stationary phase. The pellet-density-limit disruption occurs close to the point where $p_2^{exp} \approx p_2^{crit}$. This disruption very often does not destroy the plasma but only reduces the central particle and energy content. It is then followed by a sequence of similar disruptions while p_2^{exp} stays critical.

A theoretically more rigorous analysis was carried out for five points of time of ASDEX shot #18716 between $t = 1.403s$ and $t = 2.030s$ using two-dimensional MHD equilibria for ideal ballooning stability calculations. Data values for current density and pressure in cylindrical approximation were used for the computation of these equilibria associating the normalized small radius r/a with the plasma volume V by $r/a = \sqrt{V/V_p}$, where V_p is the total plasma volume. Although the detailed ballooning analysis of this time sequence reveals that the actual local β_p-value $\beta_p = (dp/d\Psi)(dV/dI)$ (Ψ poloidal flux, I toroidal current) is always less than the critical one for marginal stability, the calculated radial profiles show a clear decrease in time. The corresponding beta-poloidal ratios in the central region of the plasma decreases by a factor of about 4 in the indicated time interval, and the ratio becomes typically about 1.3 before the internal disruption occurs.

The internal disruption caused by the central radiation is accompanied by strong MHD activity, which is probably due to m=2 modes; however, a final analysis of the mode structure was not possible. Although the internal disruption occurs close to the ideal ballooning limit in all cases investigated, a definite answer about the mechanism cannot be given.

7. Plasma Edge Phenomena

Because ASDEX is equipped with a relatively large number of plasma boundary diagnostics, one can correlate information from the boundary to the typical behaviour of LRP and HRP discharges. It is then possible to derive a certain physical understanding of the processes going on.

Direct proof that poor confinement and density build-up (LRP) are correlated to low recycling and vice-versa can be obtained by measuring the flux density of neutrals Γ_n in the divertor. As shown in [21], the recycling in diverted ASDEX discharges is concentrated in the divertor. More than 90% of the particles leaving the main plasma flow into the divertor. From the flux density of neutrals measured there with encased fast pressure gauges one can derive the contribution of the recycling to the maintenance of the plasma. Since the fluxes develop quite differently in the two divertors, this depending on the main plasma density (up to a factor 2.7 higher in the lower divertor for the highest plasma densities), one has to average the values found in the two divertors. This also eliminates additional smaller variations resulting from minor vertical plasma shifts.

Figure 10 shows the averaged neutral particle flux density Γ_n for a typical LRP discharge where no successful density build-up was possible and the energy confinement was low [4]. For comparison an HRP discharge shows Γ_n values which are a factor of typically 5 to 10 higher. Whereas in HRP discharges the contribution of the recycling in the divertor to the fuelling dominates over all other external particle sources such as gas puffing, pellet injection, and neutral injection, in LRP discharges it is at most comparable to the external ones.

The effect of low and high divertor recycling on the plasma edge density can be continuously monitored by a lithium beam diagnostic. This diagnostic measures the density close to the separatrix in the midplane with a time resolution better than 1 ms [22]. Let us first discuss the observation in GP discharges. In typical GP discharges there is a strict relation between the line averaged bulk plasma density $\bar{n}_e$ and the density at the separatrix n_s. For values of $\bar{n}_e$ in the range $0.1 - 0.8 \times 10^{20}$ m^{-3} and $q \approx 3.3$, $B \approx 2.2T$, $I \approx 320kA$ the relation is $n_s = 0.3\bar{n}_e$. The factor 0.3 has a systematic uncertainty of about 20% but depends very little on the parameters of the discharge. A change in bulk plasma density is correlated to a proportional change in the boundary, and the relative exponential density decay length λ_n in the scrape-off layer does not change ($\lambda_n \approx 2cm$ for $D_2, q \approx 3, \bar{n}_e = 0.5 \times 10^{19} \ldots 3.5 \times 10^{19} m^{-3}$). This observation agrees with the assumption that particle transport is described as an inward drift $v_{in}(r)$ and diffusion $D(r)$, and that the ratio v_{in}/D, which increases to a value of $50m^{-1}$ at the separatrix, changes little with $\bar{n}_e$. The strong increase of v_{in}/D close to the boundary already becomes visible from the Thomson scattering data in the bulk (see Fig. 4.). The particle source at the boundary seems to have little influence on this situation, which should mean that a certain v_{in}/D value is realized by relatively large v_{in} and D values. At the low density limit for a constant $\lambda_n (n_s = 2 \times 10^{18} m^{-3})$ one can derive $v_{in} \gg 20m/s$ from this condition and from the bulk plasma recycling flux $\Phi \approx 4 \times 10^{19} s^{-1} m^{-2}$ [21] derive $v_{in} \gg 20m/s$. The strong increase in v_{in}/D should therefore be realized by a strong increase of v_{in}.

The situation is different in LRP discharges with low divertor recycling (see Fig. 11a): After the injection of each pellet the density inside the separatrix $n_e(r_s-2cm)$ increases, while the density outside at r_s+2cm remains about unchanged (r_s is the radius of the separatrix). In the time interval between two pellets the density at $r_s - 2$ cm decays and the profile, which is steep after injection, again becomes flat. Figure 11b shows the behaviour of n_e at the same locations for an HRP discharge. Relatively little oscillation within the pellet cycle can be found and the oscillations nearly disappear in other cases whenever the fuelling efficiency becomes $\eta_f \approx 1$. While the behaviour of HRP discharges is similar to that of GP discharges in this respect, the ratio $n_s/\bar{n}_e$ decreases from its standard value in keeping with the peaking of the bulk profile.

The observations of GP, LRP, and HRP discharges and especially from the reduction of the steep density gradient close to the separatrix immediately after injection in LRP discharges yields the following picture: the particle transport - close the the plasma boundary in the radial direction and in the scrape-off layer parallel to the field lines - is governed by fast processes. These processes determine a certain equilibrium for the density. The pellets and the associated particle flux are not able to drive the density away from the equilibrium relation.

Further detailed information can be obtained from two other boundary diagnostics: the monitor of a CIII line in front of the target plates in the divertor and a thermographic system which measures the energy flow onto the target plates as a function of time and space.

The C III line is sensitive to a certain plasma temperature T_t in front of the plates: C III can be observed if $T_t \gtrsim 10$ eV. In a discharge (see Fig. 1c) with variable gas puff phases, the C III intensity in a phase with low recycling and low filling efficiency is high, while in a period of high recycling and successful density build-up C III decreases or disappears, indicating a lower plasma temperature in front of the plates. In general, the C III line observation turned out to be a successful guide during the experimental campaign.

The thermography confirms the C III observation. In phases with high C III intensity the power deposition on the target plates shows a profile across the plates with a peak at the separatrix (see Fig. 12), while without C III this peak disappears. In both cases the total power deposition is about equal. So it seems that only in the peak region T_t is high enough to excite C III. The decrease of T_t

and the disappearance of the thermographic peak is a measure of the beginning of high recycling in front of the divertor plates.

8. Discharges with Additional Heating

In this section, pellet-fuelled discharges with neutral injection (co-injection up to 3 MW, counter-injection up to 1 MW) will be discussed.

The results with co and counter neutral injection can be summarized as follows:

a) Up to a level of 0.5 to 1.0 MW the discharge behaves very similarly to an OH discharge. HRP discharges with limited NI heating show a stepwise increase of the line-averaged density, and parallel to that an improvement of the energy confinement time by a factor of 1.2 can be found (see Fig. 13a). If pellet injection stops before a density limit disruption, a quiescent phase can be observed as in the OH case. Again, impurity accumulation leads to strong central radiation.

b) Beyond a certain heating level, but still in typical L-mode discharges, the picture changes: even with relatively strong recycling no successful density build-up is possible (see Fig. 13b). The decay of the line-averaged density after the pellet rise is due to two effects: a much faster continuous decrease and in addition pronounced sudden reductions of the line-averaged density associated with sawteeth. The energy confinement time is not improved. These discharges will be discussed in the following in more detail.

c) At a heating power of 2.5 MW the H-regime can be reached together with pellet injection. The operational regime with respect to density was extended to a density of $\bar{n}_e = 1.2 \times 10^{20} m^{-3}$ in these discharges, compared with a typical upper limit of $\bar{n}_e = 0.8 \times 10^{20} m^{-3}$ with gas puffing only. Again, further details will be given later on.

In cases with high neutral injection power ($P_N \sim 1.7 MW$) where the discharge remained in the L-regime the unsuccessful density build-up is accompanied by specific MHD activity. Immediately after each pellet m=1 mode activity is triggered in the centre (SX observation) and at the same time an m=4, n=1 mode can be observed by the Mirnov signal. Usually these two modes are damped out but soon start to reappear. They finally stop with the first sawtooth after the pellet (see

Fig. 14). The sawtooth leads to a distinct reduction of the line-averaged density while the total particle content seems to be conserved. It is interesting to note that this signature needs $\sim 50ms$ to build up after NI switch-on and disappears in less than 10 ms after the additional heating has been terminated.

In some cases the time difference between the pellet and the next sawtooth shrinked and the mode activity continued during these events. In the limit the sawtooth and the accompanying mass loss seem to happen immediately (that is within 1 ms) after the pellet. The sometimes observed lack of pellet particles in the plasma [23] can possibly be explained by this effect. The time resolution of the interferometer and the SX system is not fast enough to resolve the small time gap between injection and the loss of the mass.

Since the m=4 mode rotates in the beam-induced toroidal direction with the same frequency as the m=1 mode, which is related to the sawtooth and the corresponding density loss, we believe that the m=4 mode is not unstable on its own but is driven by the dominant m=1 instability. It would thus be produced by coupling through the poloidal asymmetries arising from the toroidal effects or from the deviations of the flux surfaces from a circular shape. As the cylindrical $q(a)$ value was 2.7, the resonant $q_\Psi = 4$ surface in these discharges was situated very close to the separatrix. In this region, too, the ASDEX divertor fields lead indeed to strong poloidal asymmetries in the flux surfaces, which, owing to the inward displacement of the stagnation points with respect to the plasma axis and owing to the combination with toroidal effects, will also have the $m = 3$ component necessary to accomplish the above-mentioned coupling.

It was possible to analyze the $n_e(r)$ and $T_e(r)$ profiles during the pellet cycle. During a period of nearly constant density (averaged over a cycle) the YAG profiles were selected and ordered according to their time gap to the last pellet and to the sawtooth. The following sequence was found:

1) The T_e profile was very peaked before the sawtooth ($T_e(0)/T_e(a/2) \approx 2.3$) and $T_e(0)$ dropped by 30% during the sawtooth. $T_e(0)$ then started to rise again. The pellet cooled the plasma only outside $r \geq 15$ cm. This indication of good isolation at the q=1 zone ($r_{q=1} \approx 12cm$) is very much in contrast to the OH cases, where very soon after injection a self-similar T_e profile was re-established [24]. Averaged over the cycle, $T_e(r)$ was considerably more peaked than in the OH-heated HRP discharges.

2) The n_e profile showed a transport of particles from inside $r_{q=1}$ to the region $r_{q=1} \leq r \leq 30cm$ in each sawtooth. This sudden ejection of particles was superposed on a continuous total loss of particles during the cycle with simultaneous peaking. At the same heating power the density in the cycle average could be increased somewhat if gas puffing was increased. However, the density build-up was much less successful than in OH discharges with the same divertor recycling. A discussion of possible reasons for the different particle behaviour will follow in Sec. 9b.

In the H-regime of a discharge ($P_{NI} = 2.7\ MW, B_t = 2.3\ T, I_p = 380\ kA$, penetration depth of pellet $\approx 12cm$) the situation with respect to the particle transport changed again: density build-up takes place typically for the H-phase even without gas-puffing and in between the pellet cycles. Starting at $\bar{n}_e = 0.85 \times 10^{20} m^{-3}$, the density could be increased to $\bar{n}_e = 1.2 \times 10^{20} m^{-3}$ by pellets and the intrinsic H-transition. The density profiles showed the typical H-type shoulders, and no pronounced density profile peaking ($n_e(0)/\bar{n}_e = 1.25$).

Very strong impurity accumulation and central radiation were found in all cases with pellet injection in the H-phase. The temperature profile got very flat and was nearly constant within the inner half-radius. There was no sawtooth activity. Typical values of the energy confinement time were 70 ms at $\bar{n}_e = 0.5 \times 10^{20} m^{-3}$ and 40 ms at $1.2 \times 10^{20} m^{-3}$, without correction for the radiation. If the radiation is taken into account, the latter value increases by 40%.

9. Discussion

The following discussion deals with essentially three topics: the plasma edge and divertor relations (Sec. 9a), the bulk plasma particle confinement (Sec. 9b), and the bulk plasma energy confinement (Sec. 9c).

9a. Plasma edge and divertor relations

The central particle and energy confinement in pellet-fuelled discharges obviously depends strongly on the edge and divertor conditioning as shown in the preceding sections, which means that the discharge does not behave essentially differently in this aspect to discharges fuelled by gas puff alone. In this section we try to clarify what edge conditioning means in terms of physical quantities, especially how the separatrix density is determined by gas puff and divertor recycling. In fact, simple analytic models [25] for the high-recycling divertor scrape-off layer show that the neutral density in the divertor together with the power input into the divertor determine the edge density in the main chamber in a non-trivial way. Even simpler relations hold for the low recycling (limiter-like) limit, while the transition region is quite complicated, regularly requiring a numerical treatment. In this context, high divertor recycling means that the total ionization flux in the divertor chamber is large compared with the inflow from the main chamber, i.e. there is a large particle flux amplification. In the opposite limit, ionization in the divertor is negligible and the amplification factor is close to one. Obviously, it depends on the neutral gas density in the divertor, i.e. on the net particle influx and the wall saturation, which case is actually obtained. Main chamber recycling is usually small in a divertor experiment like ASDEX since most of the ion loss is "diverted" into the separate chamber. We shall see, however, that at high density the neutral backflow from the divertor can be quite substantial.

The general divertor scrape-off layer behaviour outlined above has been confirmed by simulations for ASDEX gas puff discharges in [26] using the SOLID one-dimensional hydrodynamic code together with a simple neutral gas recycling model (checked qualitatively against a full Monte Carlo description).

This study is being extended at present by routinely using the two-dimensional DEGAS Monte Carlo code making detailed comparisons with various improved divertor diagnostics now available. Detailed results will be given elsewhere. Here we just concentrate on the relation between the midplane separatrix density and the neutral gas flux in the divertor. We shall compare the calculations with experimental results obtained with and without pellet injection. Figure 15 shows the separatrix density n_s determined from the lithium beam diagnostic as a function of the neutral gas flux Γ_n in the divertor outside the plasma fan measured by the above-mentioned gauge. Data are taken at various times from several ohmic deuterium shots with titanium evaporation in the divertor dome. In two discharges (#19566, #19569) the density is increased by gas puff to a high plateau value and then pellets are injected as discussed earlier, while the third one (#19514) is finally driven into a density limit disruption by gas puff only. An ohmic shot (#19554) staying at low density is also included. Except for the latter case high Γ_n values therefore correspond to the late phase of the discharge, i.e. the plateau and pellet phase, while low values ($< 10^{21}\,\mathrm{m}^{-2}\,\mathrm{s}^{-1}$) refer to the initial density rise. Obviously, all data fall roughly on the same curve in spite of the different fuelling and the unique relation predicted between the two quantities is experimentally confirmed.

During the density and current plateau the ohmic input is above 500 kW and the power radiated in the main chamber is roughly 200 kW, leaving 300 kW as input into the scrape-off layer. Of that about 200 kW is radiated in the divertor, with substantial up-down asymmetry towards the end, indicating some difference in the final divertor wall saturation on an intrinsic up-down asymmetry of the confinement in the edge region. Target plate thermography gives a total target load of about 50 kW or less in this phase, yielding a reasonable total power balance. The ratio of the electron to ion input power into the scrape-off layer is taken from an interpretation code, but is somewhat uncertain.

Taking these data together with the magnetic field topology and assuming a radial scrape-off layer width of 1 cm in the midplane, the heat flux parallel to field lines to be used in the simulation is $q_{\|} \approx 1\,\mathrm{to} 1.5 \times 10^{7} W m^{-2}$ in the current plateau. During the initial slow current rise it is correspondingly lower. With these prescriptions, essentially two free parameters remain as input for the simulation, the gettering coefficient in the divertor and the ion influx from the main chamber. The backflow of neutrals into the main chamber is self-consistently calculated and external pumping is negligible.

Starting from these experimental data, a series of simulation runs was made. In Fig. 15 only the most significant results and trends are presented in comparison with the experimental data. The solid lines show results for $q_{\|} = 1.2 \times 10^{7}\,\mathrm{Wm}^{-2}$ (corresponding to the plateau phase) and the dashed lines for half that value (corresponding to the initial density rise). The effect of varying the wall saturation is demonstrated by selecting two different combinations of atom and molecule gettering coefficients. Along each line the ion influx into the scrape-off layer is varied.

Hydrogen was used in the simulation instead of deuterium, causing an error of about $\sqrt{2}$. Errors of this order of magnitude are, however, also to be expected in the experimental data (differences between shots, inaccurate separatrix position, etc.). If this is kept in mind, the lowest gettering fits reasonably at the higher density, while at lower n_s and Γ_n an increasingly higher gettering is obviously required to reproduce the experimental data. It is recalled that the input power is also lower there. The absolute gettering coefficients are quite realistic for titanium evaporation. Despite the variation of Γ_n over two orders of magnitude, the total calculated wall pumping flux (a few times $10^{21}s^{-1}$) changes only gradually along the experimental curve because of the opposite trend of the wall saturation. A flux of this order will in fact be able to saturate the divertor walls in a fraction of the typical discharge duration of a few seconds. The backflow of neutrals from the divertor into the main chamber, however, increases monotonically with Γ_n and becomes comparable at the end with the decreasing external gas puff. The plasma temperature before the target plates decreases with rising Γ_n from $> 30eV$ at low n_s to a few eV at high n_s. Separate runs of SOLID with trace impurities also show that C III at the target is strongly reduced below 10 eV. These numerical results are in line with the experimental trends described above and in earlier papers [21, 27, 28], indicating the relevance of our physical and numerical models.

All in all, we find that edge conditioning mainly means providing the appropriate separatrix electron density n_s in the midplane, in the sense that increasing divertor recycling at given power input in the scrape-off layer causes the edge density to increase. The divertor recycling in turn depends on the previous history of the discharge. In this picture, it would be the edge density which determines the central particle confinement with pellet injection.

9b. Bulk plasma particle confinement

While with respect to the boundary a pellet-fuelled discharge depends on the same boundary equilibrium relations as gas-fuelled discharges, this is not the case for the central plasma. Peaked density profiles are correlated to a change in particle transport. This change always goes together with a reduction and, finally, the disappearance of the sawtooth activity. The neoclassical q-profile shows in parallel a small but significant increase of q(0) (see Fig. 16). There are two reasons for the reduction of the current density on axis:

1) The $T_e(r)$ profile in some discharges already flattens early during injection, but in any case later when the central radiation rises.

2) The increase of density around half the radius by the ablated material increases the collisionality. This reduces the local resistivity enhancement due to the trapped particles.

It is interesting to note that the temperature profile in typical HRP discharges is never made more peaked by the injection, although most of the pellet material is ablated around half the radius and has to be warmed up there. In these discharges there seems to be fast energy transport (time scale $< 1ms$), out of the centre into the ablation region, which tries to keep the temperature profile self-similar. In TFR [24] this transport was nicely observed as a cooling wave travelling in front of the pellet. An energy transport channel out of the centre is therefore opened up by the pellets parallel to the sawtooth activity. Besides the q-profile, this can be taken as a separate argument for reducing the influence of the sawtooth activity.

This leaves the question how the reduced sawtooth activity influences the particle transport. In a separate investigation [29] the particle transport in a normal discharge by the sawtooth itself was investigated. By combining the information from the HCN interferometry and the YAG laser system significant transport data could be obtained. Fast outward transport by the sawtooth is balanced by a continuous inward drift in between two sawteeth with a maximum flow of the order of $\Gamma_e \approx 0.5$ to $1.0 \times 10^{21} m^{-2} s^{-2}$ at around 40% of the radius but extending at least to the outside up to r=2/3a. The maximum flow corresponds to an inward velocity of $v_{in} \approx 0.2 - 0.3$m/s at r=0.4a. The inward flow velocity observed (see Fig. 5b) in HRP discharges is at r=0.4a very close to this value (see Sec. 4) and can be seen as the normal inward flow unbalanced by the sawtooth outward ejection.

This view of the reason for the profile peaking can be supported by observations in two different situations:

1) peaking in sawtooth-free discharges without pellets, and

2) absence of peaking in high-power L-discharges with pellet injection.

Sawtooth-free phases were observed in ASDEX in two different cases. In the normal ramp-up phase sawteeth first appear after the so-called "ereignis" [30]. Long phases without sawteeth where obtained in a specifically investigated discharge with a current rising in steps [31]. In both cases the $n_e(r)$ profile peaked beyond the standard profile. The reason for the non-appearance of sawteeth in these cases was a combination of the skin effect and central radiation.

In the high-power L-mode discharges with pellets (see Sec. 8) sawtooth activity did not vanish but became even more intense and no density peaking and density build-up was found. These discharges are characterized by a relatively peaked $T_e(r)$ profile and a low value for $q(0) \approx 0.75$ which does not come close to 1 during injection (see Fig. 16). This situation seems to stabilize, because the $T_e(r)$ does not remain self-similar after injection but drops at half the radius with little change in the centre. For these low q(0) values the zone with q=1 seems to isolate the centre well until a sawtooth transports energy together with particles out of the centre. The primary cause of this behaviour could be twofold: firstly, at these higher T_e values ($T_e(a/2) \approx 850eV$ instead of $T_e(a/2) \approx 450eV$ in OH discharges) the pellets cannot drive the collisionality back into the collisional Pfirsch-Schlüter regime. The second and probably most important reason may lie in the bad particle confinement at the boundary in the L-mode. There are indications that under L-mode conditions we have not really reached the HRP condition with sufficient recycling level for this case. The missing sufficiently high divertor recycling could lead to a continuous loss of particles and energy. In this respect the characteristic sawtooth and MHD activity would only be a secondary effect due to convection cooling in the outer part of the plasma.

A peaked density profile as the "natural" profile calls for an anomalous inward drift of the order $v_{in} \approx 1m/s$. The Ware pinch effect with $v_{in}^{ware} \approx 0.02m/s$ in our case is much too small as an explanation. We are not able to give a final answer to this question, but we should like to add some speculative thoughts. Because it is not easy to imagine a friction force leading to an ambipolar inward drift, one has to assume a global or a proper turbulent electric field driving this motion. The fact that the inward drift seems to exist under practically all conditions and shows a spatially global character (see, for example, Fig. 6a) might favour a global E-field as an explanation. The most simple structure of a global E-field leading to an inward drift is a vertical E-field E_v opposite to the field driving the Pfirsch-Schlüter currents. Such a macroscopic electric field would correspond to a vertical displacement of the equipotential surfaces with respect to the magnetic flux surfaces, describable in a circular cross-section model to lowest order as $\Phi(r,\Theta) = \Phi_0(r) + \Phi_1(r) sin\Theta$. It would lead to a macroscopic flow in the major radius direction and - owing to toroidal effects - also to a net flow through each flux surface, with an average velocity $v_{in} = < v_r > = \Phi_1/(R_0 B_t)$. Under ASDEX conditions only a potential Φ_1 of the order of 1 V is necessary to drive the observed inward drift at r=a/2. The drift velocity seems to be very high at the boundary: $v_{in} \gg 20 m/s$ (see Sec. 7), which would call for an increase of the potential Φ_1 in the boundary to values of ≈70 V. It is not known whether thermal force or any other non-classical effect produces this potential difference.

The reformulation of Ohm's law by Haines [43] leads to another interesting aspect of the inward drift. In this formulation a term $(\frac{2}{5} q_e \times B)/p_e$ appears while the conductivity is a scalar. If we formaly replace the classical electron heat flux q_e by the observed anomalous one, one gets an inward drift of the right sign and order of magnitude out of Ohm's law.

One candidate for a turbulent inward drift is the ion-mixing mode [32]. Parallel to the anomalous outward transport of energy, particles should be transported inward. A stationary density profile should be reached when $n(r)/n(r_o)$ reaches $(T(r)/T(r_o))^{3/2}$. At the same time the instability switches off. Although, in general, peaking of $n(r)$ can be explained by this theory, the quantitative behaviour of $n(r)/n(r_o)$ deviates from the above expression especially in the centre when $T(r)$ gets flat and n(r) shows distinct peaking.

Besides the deuterons (or protons), high-Z ions also show a pronounced inward drift of $v_{in}^{(Z)} \leq 5 m/s$ and a relatively small D value of $\approx 0.05 m^2/s$. Compared with the background plasma, their equilibrium profile is therefore more strongly peaked and it is more sensitive to the sawtooth activity. In contrast to the background ions, the impurities can move inward owing to the friction with the main plasma ions (neoclassical transport). A quantitative analysis based on neoclassical theory according to Hirshman [33] (using the formulation given in [34]) yields a relatively small diffusion coefficient of $D_{neoc} \leq 0.015 m^2/s$ but a quite remarkable inward drift. The latter is composed of an inwardly directed proton density gradient term and an outwardly directed temperature gradient term which for titanium reach, respectively, the maximum values ≈ 4 m/s and -2.5 m/s. As mentioned, the observed accumulation (Fig. 8) requires inward velocities of approximately 5 m/s, which can be obtained only if we neglect the temperature gradient term (which appears to be less certain anyway) and, furthermore, add the anomalous inward drift of v_{in}=0.7 (r/a) m/s. It should be noted, however, that the applicability of the cited theory is questionable for several reasons, on the one hand, neglected terms such as those caused by rotation (inertia) and viscosity might not be small [35] and, on the other hand, the self-interaction of the impurities becomes dominant ($\alpha = Z^2 n_Z / n_i \gg 1$), so that the theory is used beyond its range of validity. In any case, if the deuterons are driven by an anomalous E-field to the centre, the same field should drive the impurities inward superposing the neoclassical effect.

9c. Bulk plasma energy confinement

A theoretical model of energy confinement in ohmic discharges has to explain the different regimes experimentally observed in ASDEX:

(1) the low-density one with $\tau_E \sim n_e$,

(2) the medium to high-density one with flat density profiles and $\tau_E \neq f(n_e)$,

(3) the medium to high-density one with peaked n_e profiles and a continuous increase of τ_E with n_e (HRP discharges).

At present, this seems alternatively possible both with a "local" model for conductive electron energy transport, and with one involving the assumption of global profile consistency.

To examine the first type of explanation, we studied the energy transport in ohmically-heated discharges with the TRANSP code [36], limiting the analyses to the quasistationary phases preceding and following the injection of a string of pellets.

Lacking a measurement of the detailed ion temperature profile, we assume a given, spatially constant enhancement factor of χ_i over the theoretical result for $\chi_{i,neoc}$ of Chang and Hinton[37], checking the resulting T_i profiles for their compatibility with the available β_{pol}, neutron production and charge-exchange measurements.

The TRANSP analyses use the following input data:

- the electron density profiles $n_e(r,t)$ measured by a 4-channel HCN laser interferometer and a 16-spatial-channel multi-pulse Thomson scattering system providing profiles every 17 ms,
- the electron temperature profiles $T_e(r,t)$ from a 4-channel ECE diagnostic and a multi-pulse Thomson scattering system,

- the bolometrically measured profiles of the radiation losses
- and global parameters such as the loop voltage V_L, plasma current I_p, diamagnetic flux measurements of $\beta_{p\perp}$, and $\beta_{p\|} + l_i/2$ as deduced from poloidal field and flux probes.

The analysis then yields the spatial variation of the radial energy fluxes in the different transport channels (ion and electron conductive and convective transport, radiation and CX losses). The conductive electron energy heat flux $q_{e,cond}$, as given by the TRANSP analysis, can also be used to define a formal heat conduction coefficient $\chi_e = -q_{e,cond}/(n_e k dT_e/dr)$. Figure 17a shows the loss channel distribution for the quasi-stationary post-pellet phase of discharge #18716 for $\chi_i = \chi_{i,neoc}$. In this situation of very peaked density profiles and favourable energy confinement, neoclassical ion losses account for 40% of the total, non-radiated power flow at a representative position (r = 2a/3) and for an even larger fraction in the central plasma. The ohmic heating power was determined from the calculated current density distribution, with neoclassical resistivity and $Z_{eff} \approx 1.3$ being used to match the measured loop voltage. Figure 17b gives the resulting ion and electron heat diffusivities. Also shown on this graph is the heat diffusivity as predicted by the ohmic transport model of Coppi, Mazzucato [38] and Gruber [39] (χ_{CMG}), which gives reasonable agreement, considering that electron heat conduction losses in the central plasma constitute in this situation a relatively small residual with consequently large error bars. Other data (neutron flux and β_{pol}) are in good agreement with these results, but are not very discriminating owing to the strong collisional coupling of ions and electrons at these high densities.

Figures 18a and 18b show the resulting χ_e values at the radius r = 2a/3 for different examples - and hence different $\bar{n}_e$ values - in discharges #18700, #18716 and others, analyzed under the assumptions $\chi_i = \chi_{i,neoc}$ (18a) and $\chi_i = 3\chi_{i,neoc}$ (18b) and plotted versus the local value of n_e (2a/3).

The first case shows that purely neoclassical ion losses alone cannot account for the roll-over observed in gas-fuelled discharges: a deterioration of electron confinement, illustrated by growing enhancement of χ_e over χ_{CMG} and χ_{neo-A} (the latter taken in the form given in [40] but with a coefficient reduced by 1/3 to fit the ASDEX low-density data) with increasing density, would also be required. Also shown are the predicted peak ion temperatures. Passive and active CX measurements do not exist for these, but for other gas-fuelled discharges with the same macroscopic parameters. Over the density range shown, the predicted $T_i(0)$ are above the upper end of the experimental error bars. We therefore consider that the explanation of the observed τ_E roll-over purely in terms of a changing density dependence of the electron confinement implied, by Fig. 18a, is less plausible, though not strictly disproved. For the peaked density profile situation, following pellet injection, on the other hand, $\chi_i = \chi_{i,neoc}$ has to be satisfied with a small margin of uncertainty (see also Fig. 17b).

Figure 18b illustrates the alternative explanation of the observed behaviour in gas-fuelled discharges in terms of an enhancement of χ_i over its neoclassical value. It shows that low and high-density results could be brought well into line with a continuous explanation of electron losses through χ_{CMG} or χ_{neo-A} by a constant enhancement of χ_i by a factor of 3 over its neoclassical value. The LRP discharges [4] also fit into this picture. Clearly, however, the effect causing the ion transport enhancement has to be quenched by the changes - presumably to the density profile - brought about by pellet injection (HRP): $\chi_i = 3\chi_{i,neoc}$ would require a negative electron heat conductivity to satisfy the global energy balance.

Figures 17 and 18 show that the observed confinement behaviour in gas- fuelled and pellet-fuelled discharges at different densities can be explained in terms of a local heat transport model following essentially the lines first suggested by the Alcator team. According to their model one has to add to the usual electron heat conduction channel dominating at low densities and to the neoclassical ion energy losses as given by Chang-Hinton an additional heat conductivity contribution independent of density (or increasing with it), triggered by η_e or η_i ($\eta = d\ell nT/d\ell nn$) and acting on either the ion or electron energy loss channel. With these three loss channels superposed, the roll-over of $\tau_E(n)$ in gas-fuelled discharges would thus be caused by the increasing dominance of the η driven mode. The peaking of the density profiles triggered by pellet injection would then quench this mode, allowing τ_E to continue to rise until it becomes affected at much higher densities by the neoclassical ion losses. A possible candidate for causing this changing behaviour would be the so-called ion temperature gradient mode, which, however, in its present theoretical form [41] has the wrong dependence on the ion mass (χ_η increasing with μ) to explain the isotope dependence of the τ_E saturation in gas-fuelled discharges.

An alternative explanation, also compatible with experimental observations, follows the profile consistency model of Furth [42]. According to it, $T_e(r)/T_e(0)$ in the bulk of the plasma is fixed by stability restrictions and only depends on q_a, whereas the normalization constant is determined by local transport processes in a near-boundary zone. In fact, $T_e(r)/T_e(0)$ profiles remain remarkably constant throughout all three regimes. When τ_E is written as

$$\tau_E = \frac{6R_0\pi^2 kT_e(0) \cdot \int n_e(r)\frac{T_e(r)}{T_e(0)}(1 + T_i(r)/T_e(r))rdr}{P_{OH}},$$

the roll-over of $\tau_E(\bar{n}_e)$ in gas-fuelled discharges follows from a decrease of $T_e(0)$ and the concomitant increase in ohmic dissipation, whereas the recovery in the pellet-fuelled ones corresponds to a more favourable weighting of $T_e(r)/T_e(0)$ with the density profile. This could be well compatible with the model of [42], according to which only edge parameters - in particular here edge densities - should determine the absolute magnitude of T_e. Whereas in gas-fuelled discharges the separatrix density $n_s(a)$ increases proportionally to $\bar{n}_e$, it remains at a nearly constant value if the latter parameter is enhanced by pellet injection.

10. Conclusions

The particle transport in gas-fuelled and pellet-fuelled discharges is ruled by two equilibrium processes: parallel to the field lines in the boundary and perpendicular to them in the bulk plasma. Neither the gas puff fluxes nor the pellet particle fluxes are able to drive the local density far away from equilibrium. However, under certain conditions the sawtooth activity can be reduced or switched off, leading to a new equilibrium profile in the bulk with peaked profiles. Together with high divertor recycling, a high particle and energy content can be built up. The energy confinement improves considerably by nearly a factor 2 and values of about 160 ms are even reached in ohmic discharges. Finally, this improved phase is terminated by impurity accumulation and strong central radiation. The phase with improved plasma performance has so far not been reached for high-heating-power L-mode discharges, while for the H-regime the upper density limit was extended.

Besides improved performance, the value of these experiments is that they make a considerable contribution to the understanding of transport in a tokamak. A final contribution of pellets to improve the plasma performance depends on solutions in two problem areas:

- Is it possible to reach the improved confinement in L-mode discharges as well?
- Is it possible to control the impurity accumulation?

The experimental programme will have to focus on these questions in the future.

Acknowledgement

The authors would like to thank F. Wagner for stimulating discussions and for contributing his broad knowledge of the ASDEX plasma. They are also grateful to O. Klüber for discussions of the MHD activity. Furthermore, the U.S. Department of Energy is thanked for supporting Z.A. Pietrzyk's work in this field.

References

[1] M. Greenwald, et al., Phys. Rev. Let. **53**, (1984), 352.
S.M. Wolfe, et al., Nucl. Fus. **26**, (1986), 329.

[2] S. Sengoku, et al., Proc. 10th Int. Conf. Plasma Physics and Contr. Nucl. Fus. Res., London 1984, **1**, (1985), 405.
S. Sengoku, et al., Nucl. Fus. **25**, (1985), 1475.

[3] W. Amenda, R.S. Lang, J. Phys. E: Sci. Instr. **19**, (1986), 970.

[4] G. Vlases, O. Gruber, et al., Nucl. Fus. **27**, (1987), 351.
O. Gruber, et al., Proc. 13th Europ. Conf. on Contr. Fus. and Plasma Heating, Schliersee, 10C, **I**, (1986), 228.

[5] J. Winter, et al., J Nucl. Mat. **122-123**, (1984), 1187.

[6] P.B. Jensen, V. Andersen, J. Phys. D: Appl. Phys. **15**, (1982), 785.

[7] O. Gehre, Course and Workshop on "Basic and Advanced Fusion Plasma Diagnostic Techniques", Varenna 1986, to be published.

[8] D. Meisel, et al., Proc. 13th Europ. Conf. on Contr. Fus. and Plasma Heating, Schliersee, 10C, **I**, (1986), 97.

[9] H.D. Murmann, et al., Proc. 13th Europ. Conf. on Contr. Fus. and Plasma Heating, Schliersee, 10C, **I**, (1986), 216.

[10] H. Röhr, et al., Proc. 13th Europ. Conf. on Contr. Fus. and Plasma Heating, Schliersee, 10C, **I**, (1986), 93.

[11] O. Gehre, et al., Proc. 13th Europ. Conf. on Contr. Fus. and Plasma Heating, Schliersee, 10C, **I**, (1986), 220.

[12] H. Niedermeyer, et al., Proc. 13th Europ. Conf. on Contr. Fus. and Plasma Heating, Schliersee, 10C, **I**, (1986), 168.

[13] H. Niedermeyer, et al., Proc. 12th Europ. Conf. on Contr. Fus. and Plasma Physics, Budapest, (1985), 9F, **I**, (1985), 159.

[14] M. Kornherr, et al., Proc. 14th Europ. Conf. on Contr. Fus. and Plasma Physics, Madrid, (1987).

[15] W. Engelhardt, Proc. Course and Workshop on Diagnostics for Fusion Reactor Conditions, Varenna, (1982), 11.

[16] C.T. Chang, K. Thomsen, Nucl. Fus. **24**, (1984), 697.

[17] K. Büchl, Bull. Am. Phys. Soc. **29**, (1984), 1367.
K. Büchl, et al., IPP-Report 1/238 (1986).

[18] K.F. Mast, et al., Proc. 14th Europ. Conf. on Contr. Fus. and Plasma Physics, Madrid, (1987).

[19] G. Fußmann, G. Janeschitz, et al., Proc. 14th Europ. Conf. on Contr. Fus. and Plasma Physics, Madrid, (1987).

[20] D. Lortz, J. Nührenberg, Nucl. Fus. **19**, (1979), 1207.

[21] G. Haas, et al., J. Nucl. Mat. **145-147**, (1987), 519.

[22] K. McCormick, J. Nucl. Mat. **145-147**, (1987), 215.

[23] K. Büchl, et al., Nucl. Fusion, to be published.

[24] Equipe TFR, Proc. 10th Int. Conf. Plasma Physics and Contr. Nucl. Fus. Res. London 1984, **1**, (1985), 103.

[25] M. Keilhacker, et al., Physica Scripta T2/2, (1982), 443.
K. Lackner, et al., Plasma Phys. **26**, (1984), 105.
M. Kaufmann, Nucl. Fus. **25**, (1985), 89.
M.F.A. Harrison, et al., Nucl. Techn./Fus. **3**, (1983), 432.

[26] W. Schneider, et al., J. Nucl. Mat. **121**, (1984), 178.

[27] G. Haas, et al., J. Nucl. Mat. **121**, (1984), 151.

[28] Y. Shimomura, et al., Nucl. Fus. **23**, (1983), 869.

[29] D. Zasche, et al., Proc. 14th Europ. Conf. on Contr. Fus. and Plasma Physics, Madrid, (1987).

[30] O. Gehre, et al., Proc. 14th Europ. Conf. on Contr. Fus. and Plasma Physics, Madrid, (1987).

[31] F. Wagner, et al., Plasma Physics **28**, (1986), 1225.

[32] B. Coppi, N. Sharky, Course and Workshop on "Physical of Plasmas Close to Thermonuclear Conditions", Varenna 1979, **1**, 47.

[33] S.P. Hirshman, et al., Phys. Fluids **19**, (1975), 155.

[34] D.E.T.F. Ashby, et al., Nucl. Fus. **21**, (1981), 811.

[35] W. Feneberg, et al., Proc. 14th Europ. Conf. on Contr. Fus. and Plasma Physics, Madrid (1987).

[36] R. Hawryluk, Course and Workshop "Physics of Plasmas Close to Thermonuclear Conditions", Varenna 1979, **1**, 19.

[37] C.S. Chang, F.L. Hinton, Phys. Fluids **25**, (1982), 1493.

[38] B. Coppi, E. Mazzucato, Phys. Let. **71A**, (1979), 397.

[39] O. Gruber, Nucl. Fus. **22**, (1982), 1349.

[40] R.J. Goldston, Plasma Phys. Contr. Fus. **26**, (1984), 87.

[41] W. Morton et al., Phys. Fluids **24**, (1981), 1077.

[42] H.P. Furth, Princeton Plasma Phys. Lab. Report PPPL-2263, (1985).

[43] M.G. Haines, Proc. 14th Europ. Conf. on Contr. Fus. and Plasma Physics, Madrid (1987), 1079.

Figure Captions

Fig. 1 The line-averaged densities $\bar{n}_e(t)$ and gas puffing in a typical LRP (Fig. 1a) and in a HRP discharge (Fig. 1b) are compared. A much more successful density build-up can be observed in the second case. In a discharge with variable gas puff (Fig. 1c) a high fuelling efficiency η_f of pellets follows the gas puff with some delay in time and becomes as large as unity for an optimal period. (Miscountings of the interferometric system in Fig. 1b are corrected by the YAG data.)

Fig. 2 Figure 2a shows the time development of the central electron temperature $T_e(0)$ and electron density $n_e(0)$ for a typical HRP discharge. The density peaking can be seen from the $n_e(0)/\bar{n}_e$ trace ($\bar{n}_e$: line averaged density). The $T_e(0)/T_e(a/2)$ curve indicates little change in the T_e profile ($T_e(a/2)$: temperature at half-radius).

Figure 2b shows the electron particle content N_e and energy content W_e together with the total energy confinement time τ_E as functions of time.

Fig. 3 Energy confinement time τ_E as a function of the line-averaged density $\bar{n}_e$ for LRP, HRP and standard ASDEX GP discharges, all of them with ohmic heating only.

Fig. 4 The density profiles and the ratios of the inward velocity to particle diffusion coefficient $v_{in}/D = n_e'/n_e$ for nearly stationary and (inside $r \approx$ 35 cm) source-free situations.

Figure 4a corresponds to the flat density profile during gas fuelling before and Fig. 4b to the peaked profile after pellet injection.

Fig. 5 Figure 5a shows the density build-up $n_e(r,t)$ by pellet injection and the subsequent phase of a peaked, nearly-stationary profile in a typical HRP discharge. The particle flux $\Gamma_e(r)$ is determined from $n_e(r,t)$ and the source $S_e(r,t)$ of ablated material (Fig. 5b). The curves correspond to the marked time intervals.

Fig. 6 Development of the density profile $n_e(r,t)$ during and after the injection of three slow pellets (Fig. 6a). The energy confinement time τ_E (Fig. 6b) as a function of $\bar{n}_e$ rises during pellet injection and reaches values which are considerably higher than the comparable GP discharges.

Fig. 7 Radiation losses as a function of time and radius in a HRP discharge (Fig. 7a) and in a GP discharge (Fig. 7b) are compared. While strong boundary radiation terminates the GP discharge by marfes strong central radiation in the HRP discharge leads to internal disruptions.

Fig. 8 Simulation of titanium accumulation during the post-pellet phase in the case of NI counter injection (Fig. 8a). The following parameters were assumed: sawtooth transport:
$\Gamma_{s,k} = v_{so} exp\{-[(t-t_k)/\tau]^2\} \times (r/r_o) exp(-r/r_o)^2$ with r_o=0.15 m, τ=1 ms, $v_{so} = 10^3$ m/s. Anomalous transport: $D_{an} = 0.05m^2/s, v_in = 0.7 \times (r/a)m/s$. Neoclassical transport according to [34] without temperature gradient terms.
Comparison between measurement and simulation for Ti XX and soft x-ray emission in the case of titanium accumulation (#20033) (Fig. 8b). The upper part of the figure shows the $\bar{n}_e$ interferometer signal and the time interval of NI injection.

Fig. 9 Comparison of the experimental value $p_2^{exp}(p(r) = p_0 - p_2 \cdot r^2)$ with p_2^{crit}, which represents the marginal value for the ballooning criterion. An internal disruption happens when $p_2^{exp} \approx p_2^{crit}$.

Fig. 10 Neutral particle flow density Γ_n in the divertor for LRP (#19539) and HRP discharges (#19569).

Fig. 11 Densities at the separatrix n_s, 2 cm inward $n_e(r_s - 2cm)$ and 2 cm outward $n_e(r_s + 2cm)$ are shown as functions of time. In the case of an LRP discharge (Fig. 11a) the density at $r_s - 2cm$ shows a steep rise after each pellet but decays immediately afterwards to its value before injection. The outer positions in the LRP case and all traces in the HRP discharge (Fig. 11b) show little oscillation with the pellet cycle.

Fig. 12 Thermographic space-resolved measurements of the energy deposition on the target plates shows characteristic differences: in the LRP situation (t=1.199 s) a peak near the separatrix appears while a broader shoulder further out is correlated to the HRP phase (t=1.600 s) during the discharge (#18881). The origin of the abscissa is the position of the separatrix calculated from magnetic data.

Fig. 13 The averaged density $\bar{n}_e$ and the energy confinement τ_e are given for an

L-mode neutral injection discharge with pellets. At a low heating power of 0.44 MW (Fig. 13a) the typical HRP signature can be found with an increase of τ_E up to 85 ms. At higher power (1.7 MW, Fig. 13b) $\bar{n}_e$ and τ_e do not increase during neutral injection.

Fig. 14 At high neutral injection power in L-mode discharges pellet injection is accompanied by specific MHD activity between the pellet injection and the sawtooth; m=4, n=1 modes can be detected by Mirnov coils, and an m=1 mode in the centre by the soft X-ray signal.

Fig. 15 Midplane separatrix density n_s as function of the neutral flux density Γ_n in the divertor chamber. Experimental data taken from several discharges are compared with SOLID-DEGAS simulations for different power input $q_{||}$ and divertor wall saturation (indicated by the gettering factors for atoms and molecules). A reasonable fit is obtained assuming strong wall pumping for low midplane density and a nearly saturated divertor close to the density limit, while there is little sensitivity to the power input in this regime.

Fig. 16 The safety factor on axis q(o) is shown for an OH-heated HRP discharge (#18716) and an NI-heated L-mode discharge (#18743). The pellet injection phase is indicated by the heavier trace. In the OH discharge case q(o) increases by about $\Delta q = 0.2$ during pellet injection while in the NI case an initial increase at a heating power of 0.86 MW vanishes at a heating power of 1.72 MW. The origin of the time scale is the start of pellet injection in both discharges.

Fig. 17 Integrated power fluxes for the different loss channels as a function of radius during the post-pellet phase of #18716 (Fig. 17a). Corresponding radial profiles of the electron (χ_e) and ion (χ_i) heat diffusivities and of the ohmic Coppi-Mazzucato-Gruber χ_e-scaling (χ_{CMG}) (Fig. 17b).

Fig. 18 Calculated electron thermal diffusivities χ_e at $r = 2/3 \cdot a$ and ion temperature T_i on axis and measured central ion temperatures as a function of the electron density n_e at $r = 2/3 \cdot a$. The analyses are performed for $\chi_i = \chi_{i,CH}$ (Fig. 18a) and $\chi_i = 3 \cdot \chi_{i,CH}$ (Fig. 18b). The scalings $\chi_e = \chi_{CMG}$ and $\chi_{Neo-Alc}$ are given too.

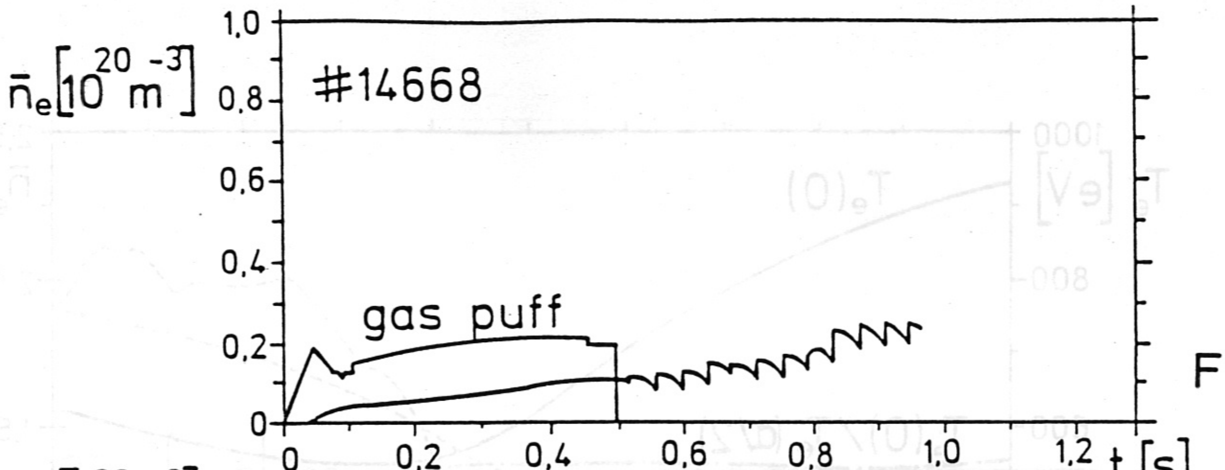

Fig. 1a

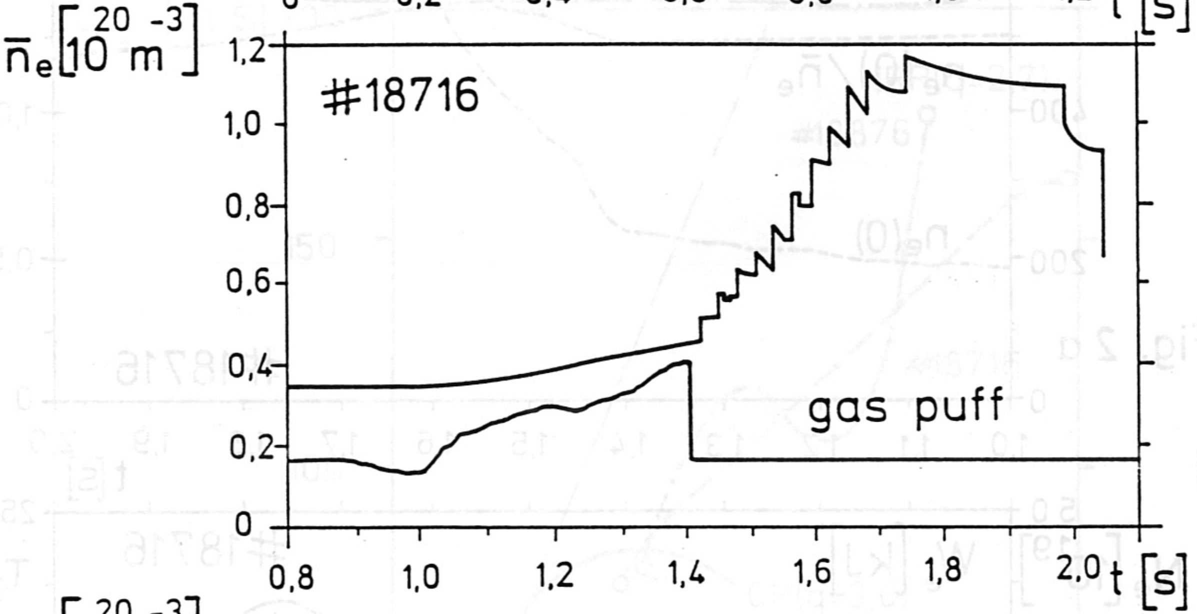

Fig. 1b

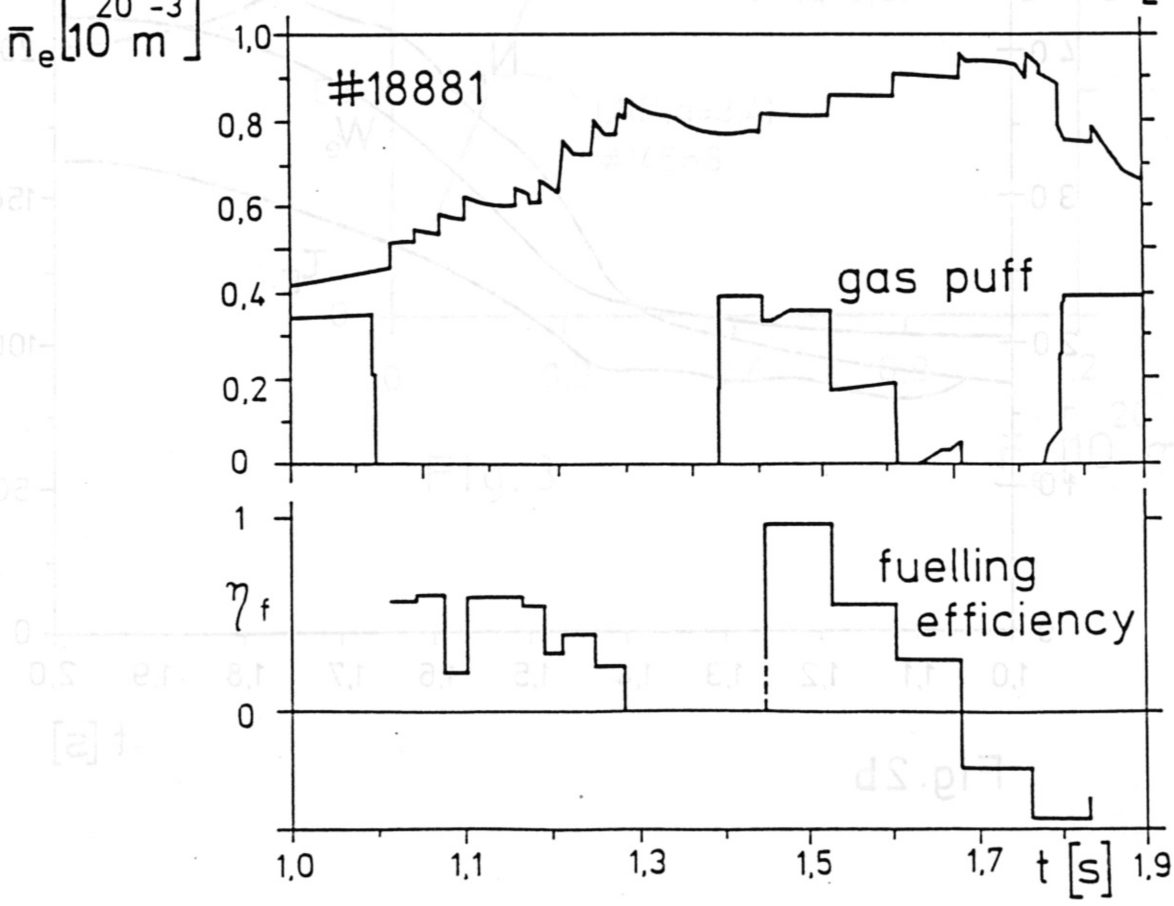

Fig. 1c

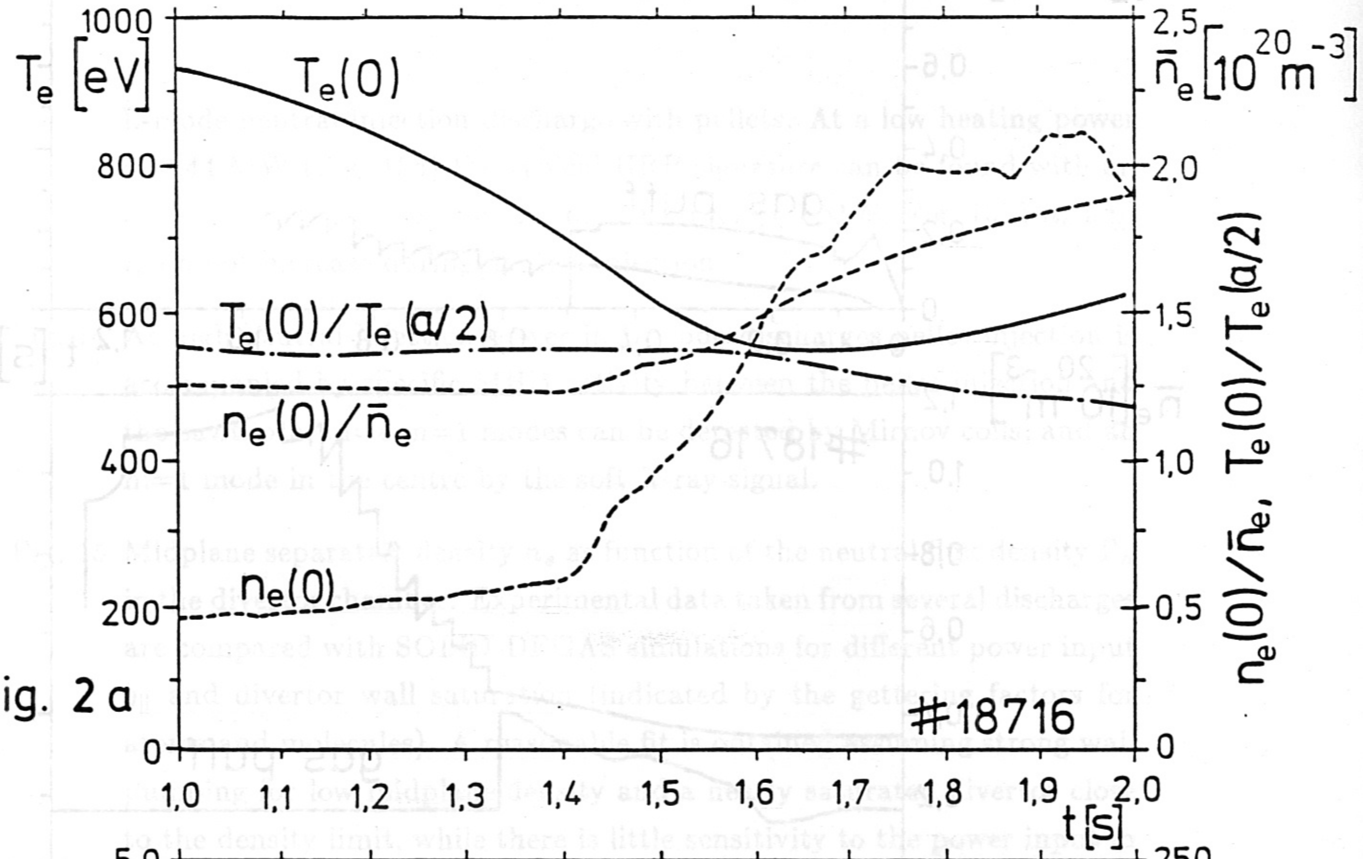
T_e [eV]
T_e(0)
T_e(0)/T_e (a/2)
n_e(0)/n̄_e
n_e(0)
n̄_e [10^20 m^-3]
n_e(0)/n̄_e, T_e(0)/T_e(a/2)
#18716
1000
800
600
400
200
0
2,5
2,0
1,5
1,0
0,5
0
1,0
1,1
1,2
1,3
1,4
1,5
1,6
1,7
1,8
1,9
2,0
t [s]

Fig. 2 a

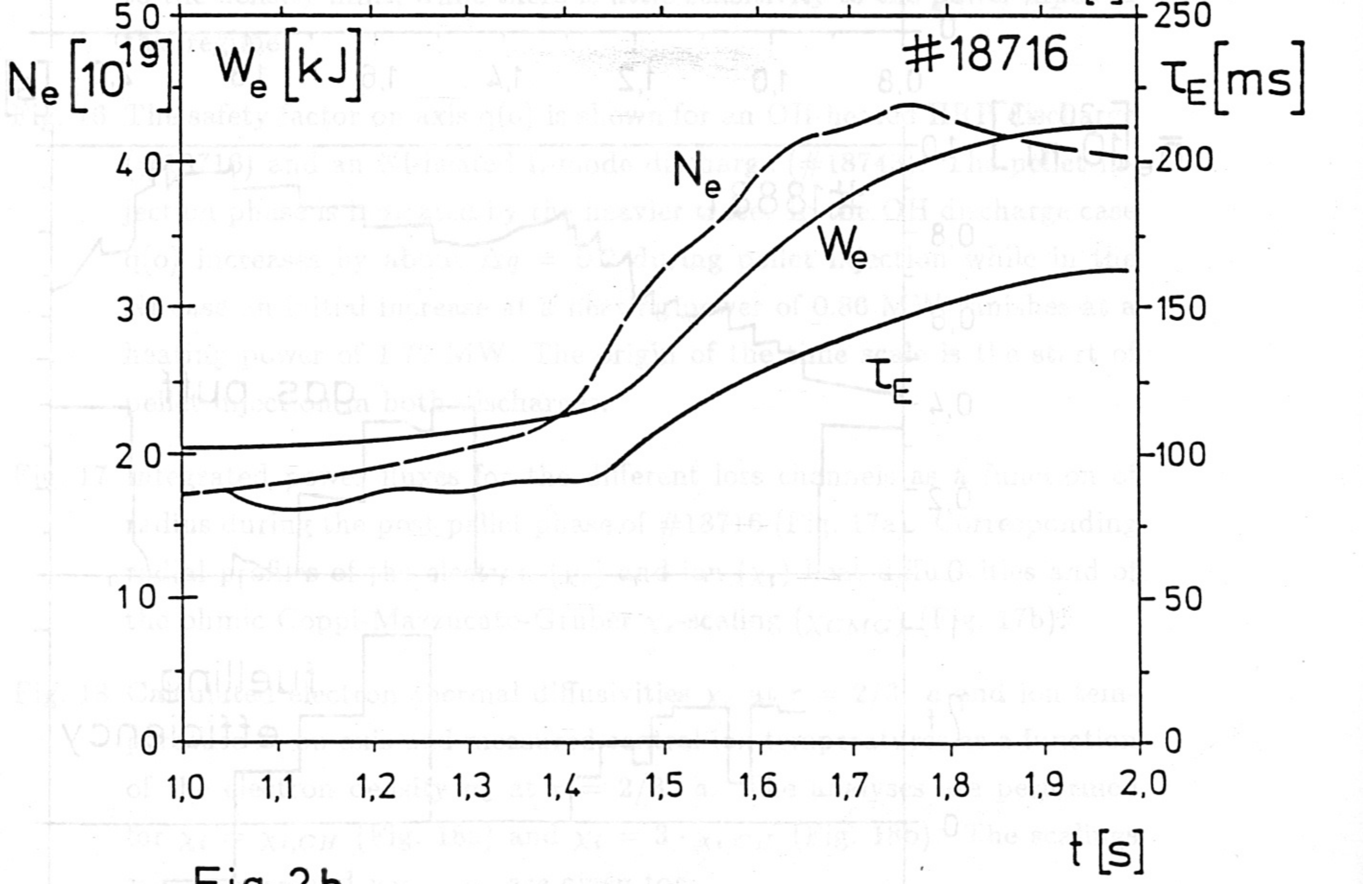
N_e [10^19]
W_e [kJ]
τ_E [ms]
#18716
N_e
W_e
τ_E
50
40
30
20
10
0
250
200
150
100
50
0
1,0
1,1
1,2
1,3
1,4
1,5
1,6
1,7
1,8
1,9
2,0
t [s]

Fig. 2b

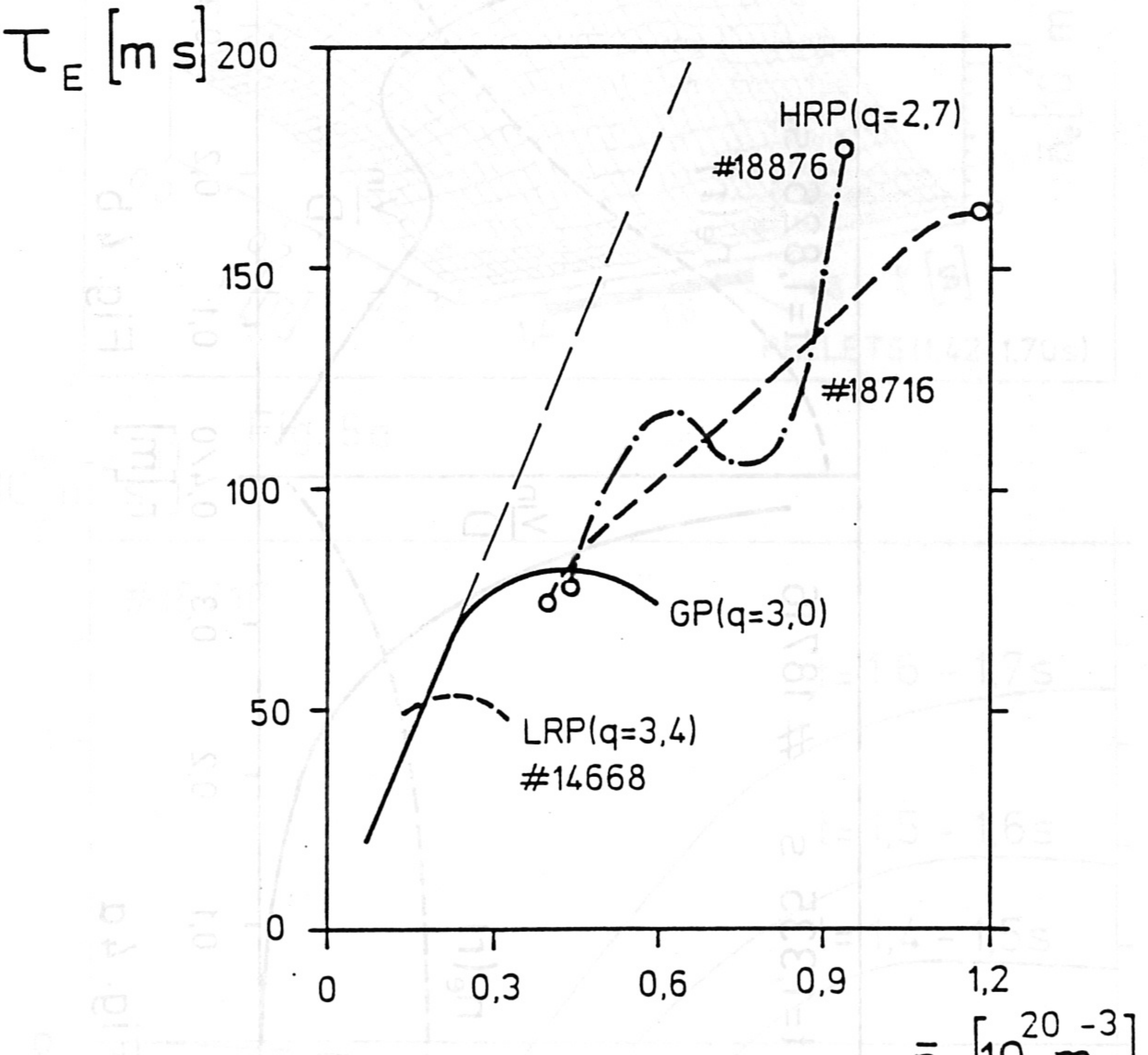
τ_E [m s]
200
150
100
50
0
0
0,3
0,6
0,9
1,2
$\bar{n}_e$ $[10^{20} m^{-3}]$
HRP(q=2,7)
#18876
#18716
GP(q=3,0)
LRP(q=3,4)
#14668

Fig. 3

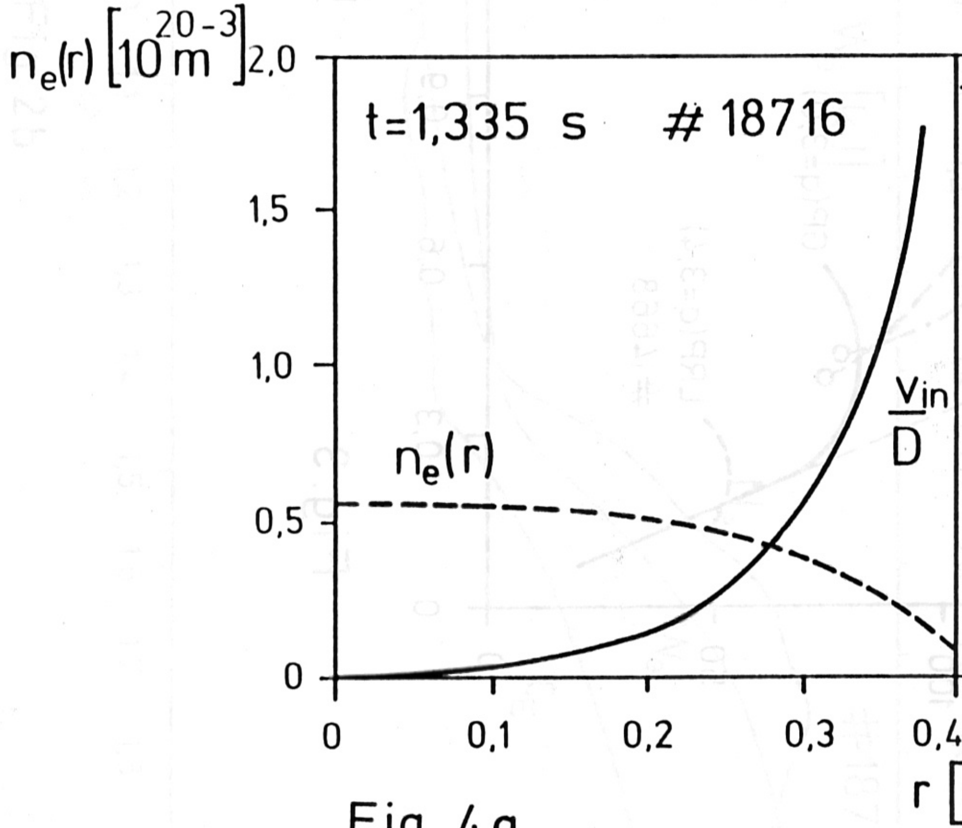
$n_e(r)$ $[10^{20}\,m^{-3}]$
2,0
1,5
1,0
0,5
0
t=1,335 s
# 18716
$n_e(r)$
$\frac{v_{in}}{D}$
0
0,1
0,2
0,3
0,4
r [m]

Fig. 4 a

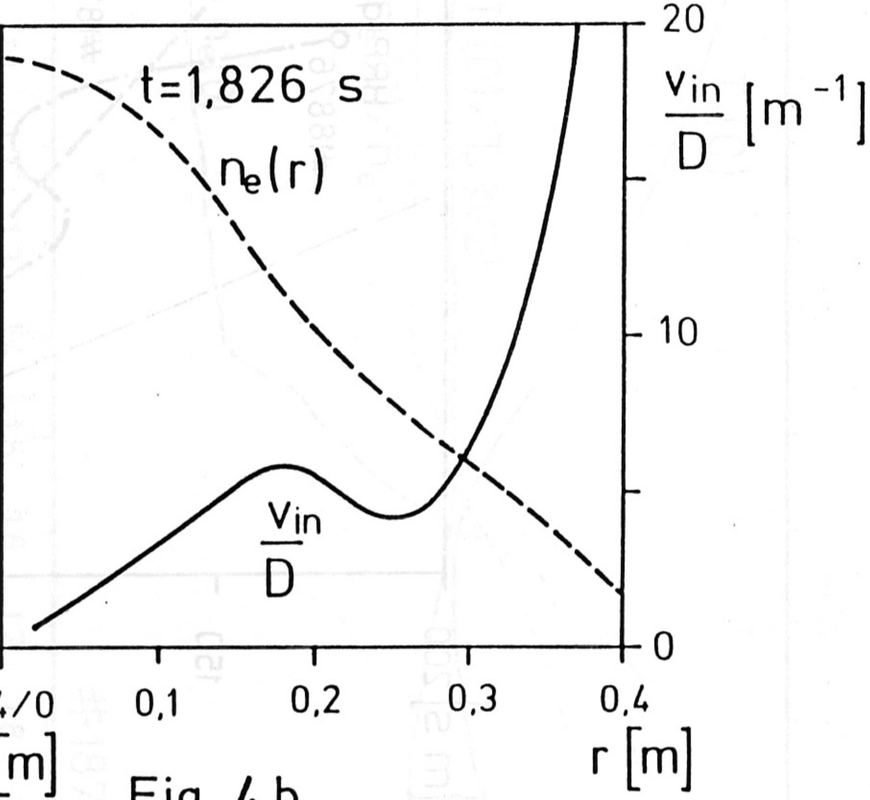
t=1,826 s
$n_e(r)$
$\frac{v_{in}}{D}$
$\frac{v_{in}}{D}$ $[m^{-1}]$
20
10
0
0
0,1
0,2
0,3
0,4
r [m]

Fig. 4 b

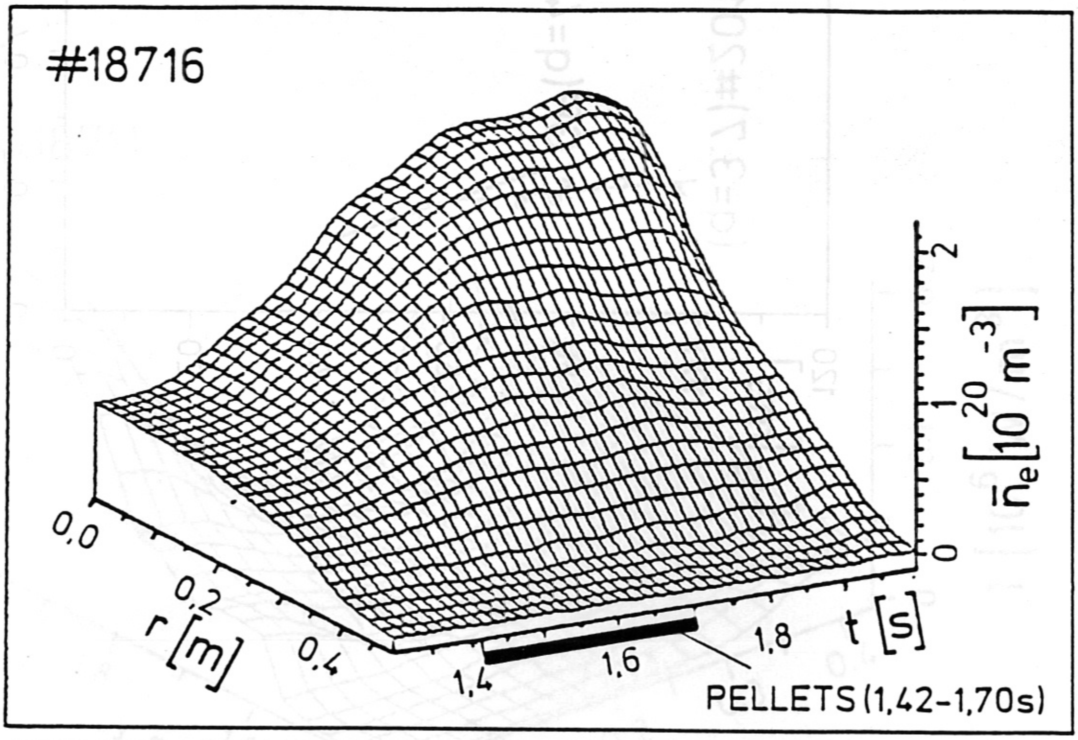
#18716
0,0
0,2
0,4
r [m]
1,4
1,6
1,8
t [s]
PELLETS (1,42–1,70s)
0
1
2
$\bar{n}_e [10^{20} m^{-3}]$

Fig. 5a

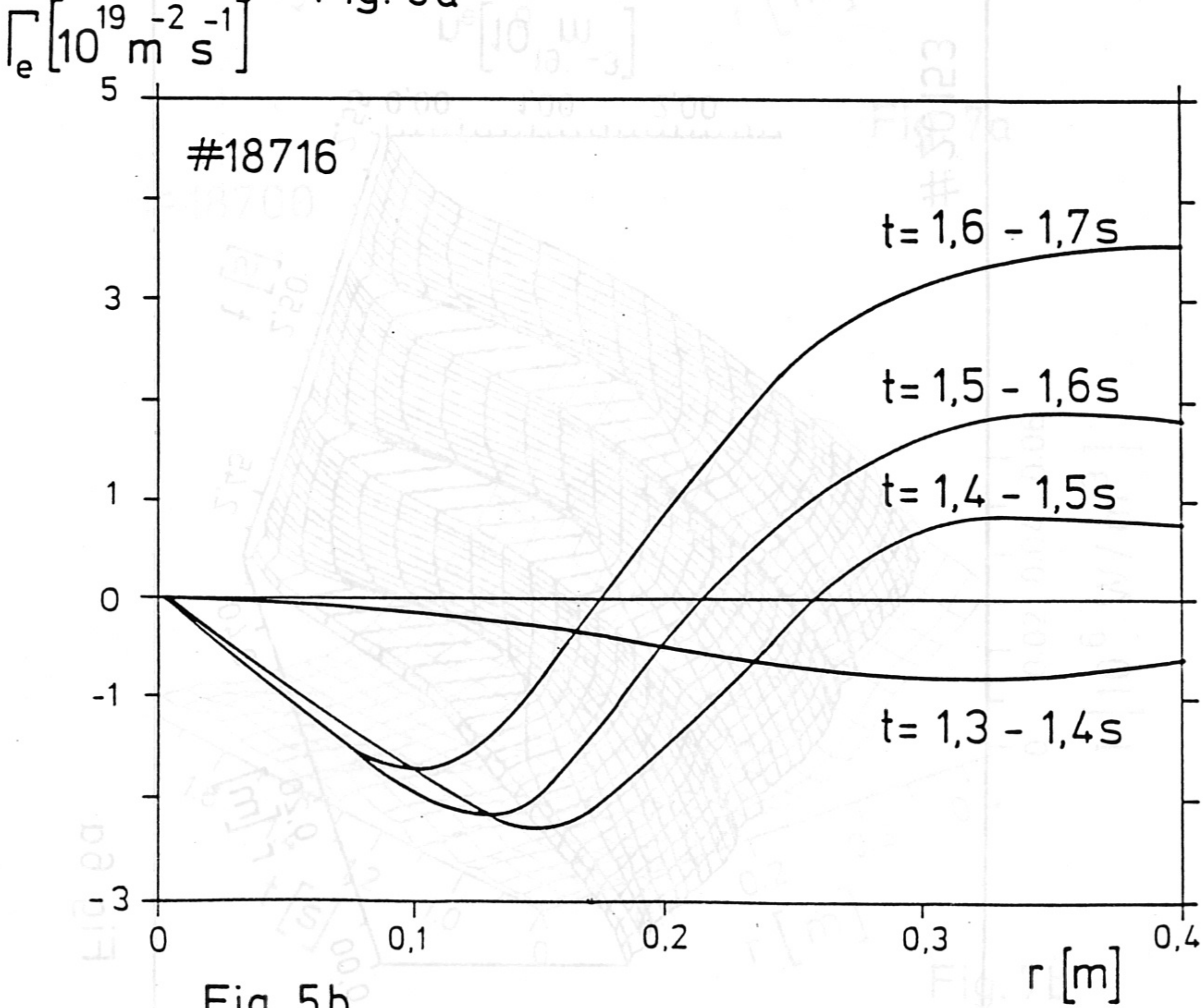
$\Gamma_e [10^{19} m^{-2} s^{-1}]$
5
3
1
0
-1
-3
#18716
t= 1,6 - 1,7s
t= 1,5 - 1,6s
t= 1,4 - 1,5s
t= 1,3 - 1,4s
0
0,1
0,2
0,3
0,4
r [m]

Fig. 5b

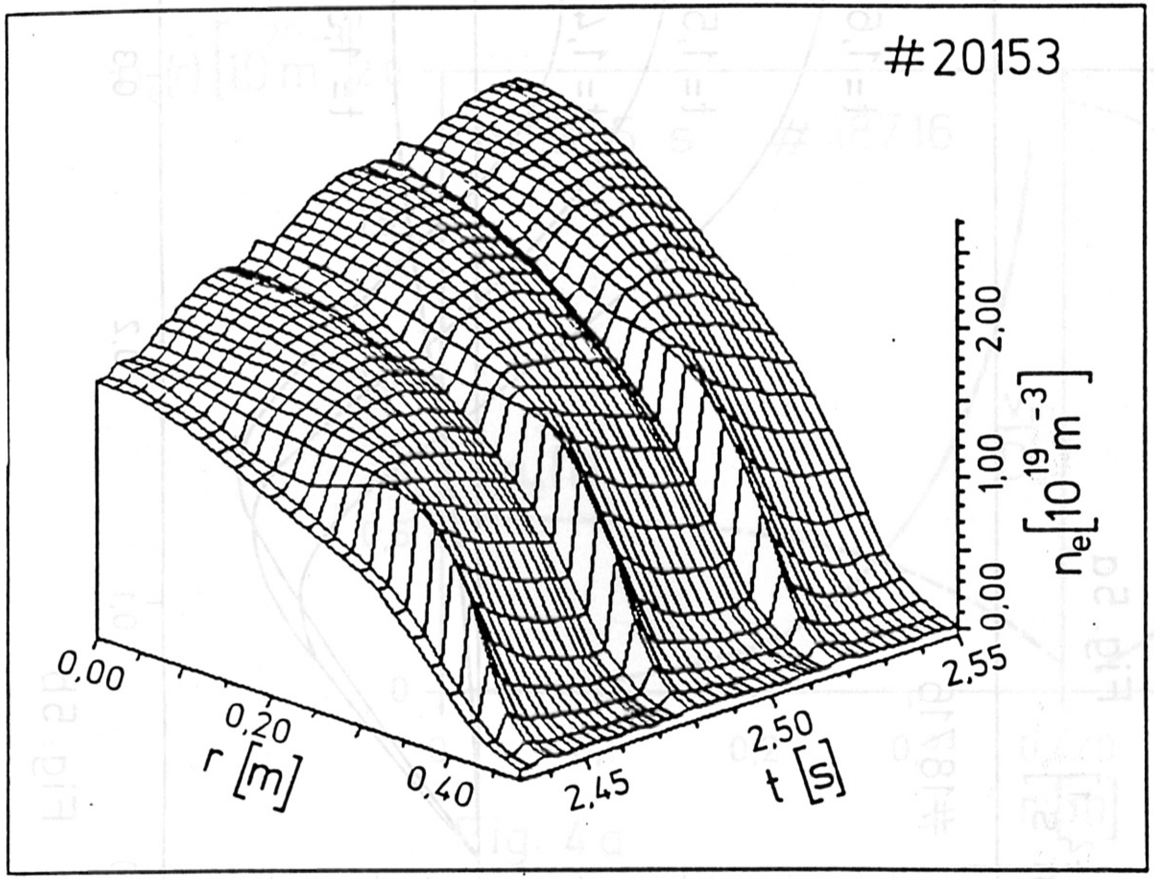
#20153
$n_e\,[10^{19}\,m^{-3}]$
0,00
1,00
2,00
r [m]
0,00
0,20
0,40
t [s]
2,45
2,50
2,55

Fig. 6a

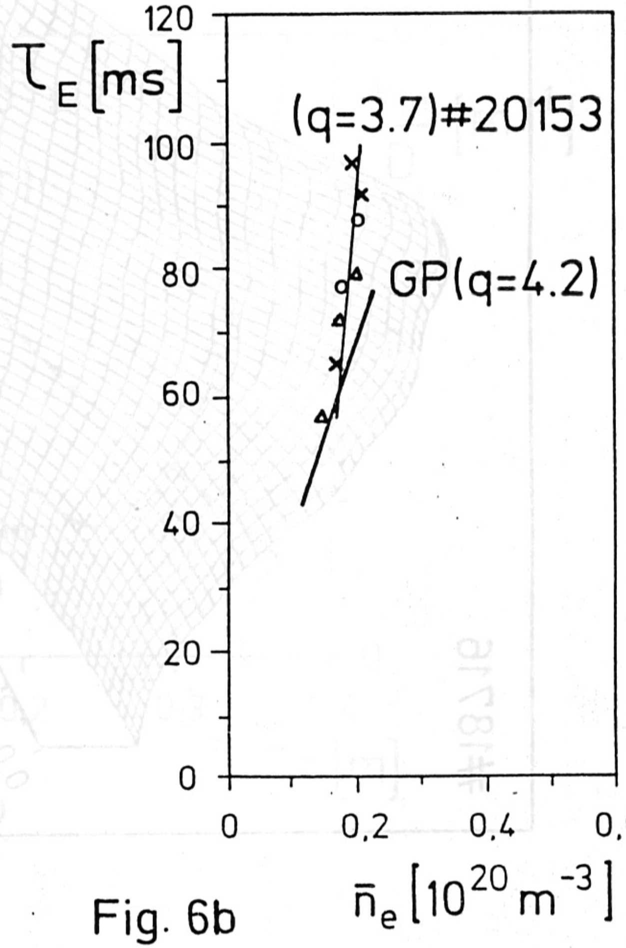
τ_E [ms]
(q=3.7)#20153
GP(q=4.2)
0
20
40
60
80
100
120
0
0,2
0,4
0,6
$\bar{n}_e\,[10^{20}\,m^{-3}]$

Fig. 6b

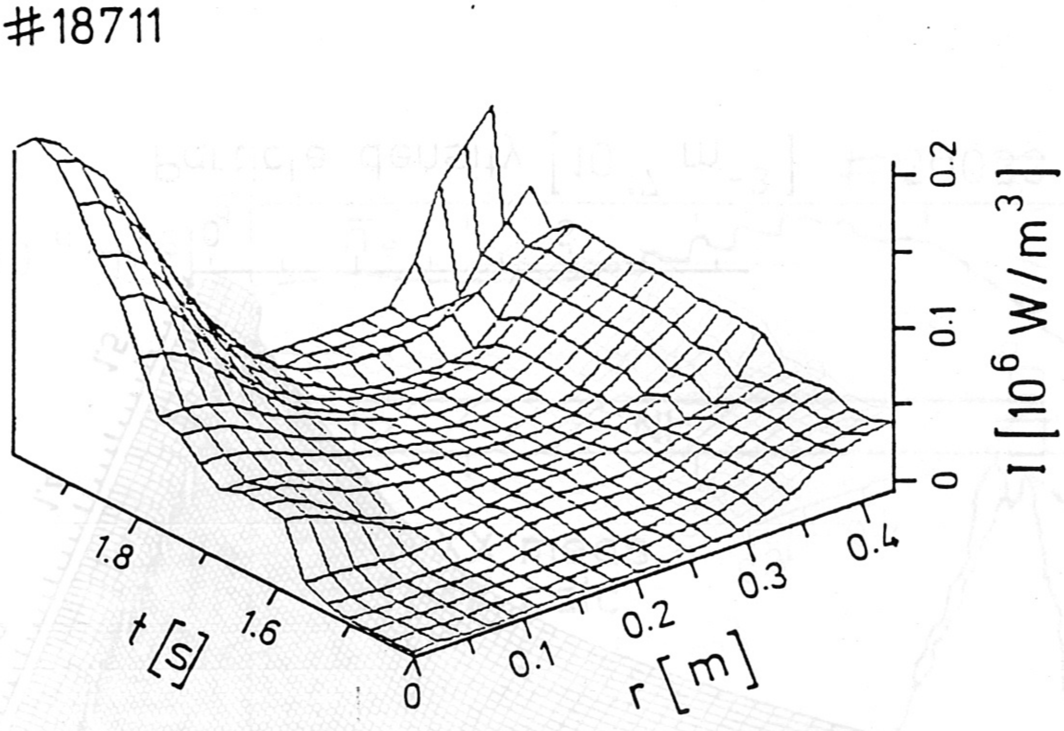
#18711
t [s]
1.8
1.6
0
0.1
0.2
0.3
0.4
r [m]
0
0.1
0.2
I [10^6 W/m^3]

Fig. 7a

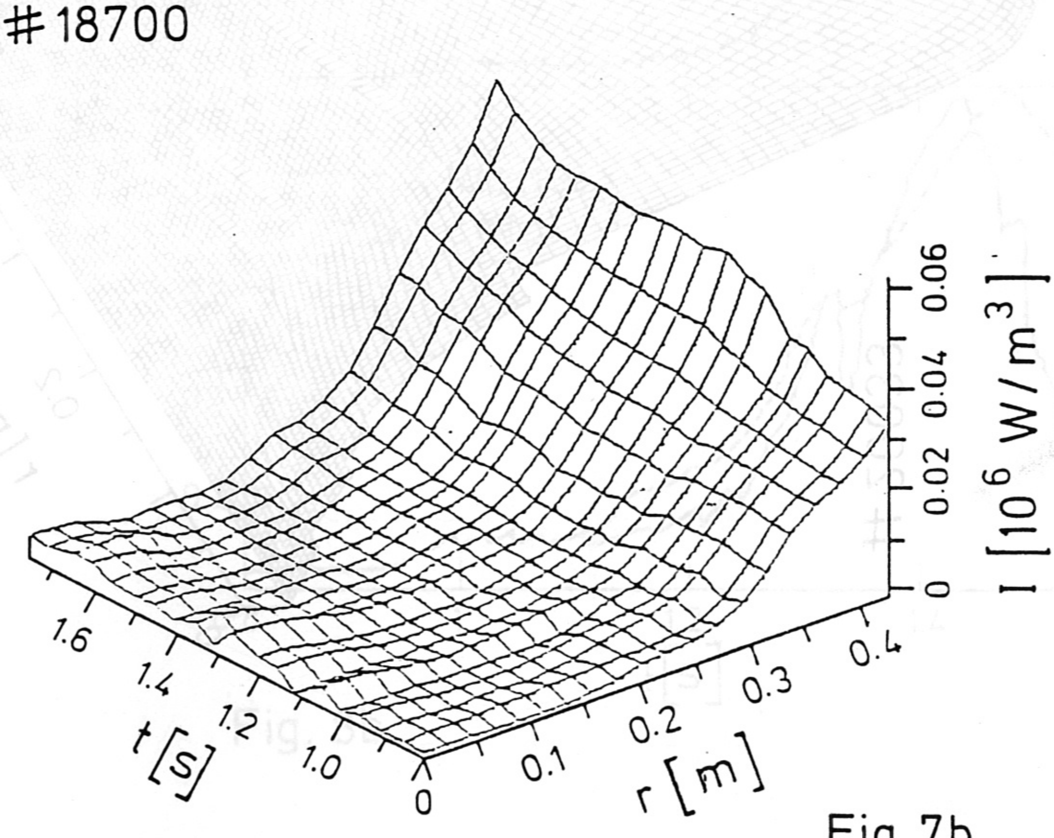
#18700
t [s]
1.6
1.4
1.2
1.0
0
0.1
0.2
0.3
0.4
r [m]
0
0.02
0.04
0.06
I [10^6 W/m^3]

Fig. 7b

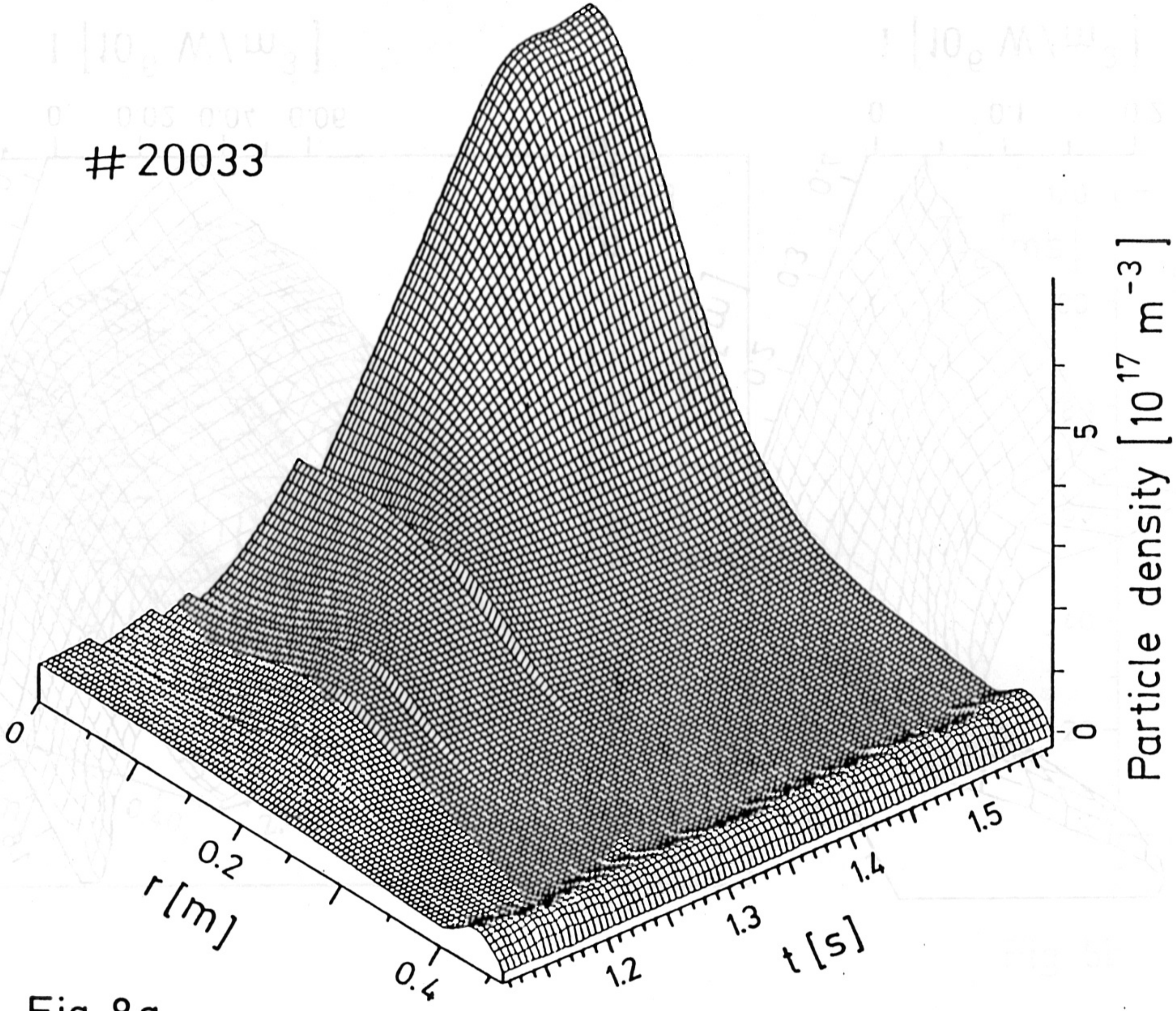

Fig. 8a

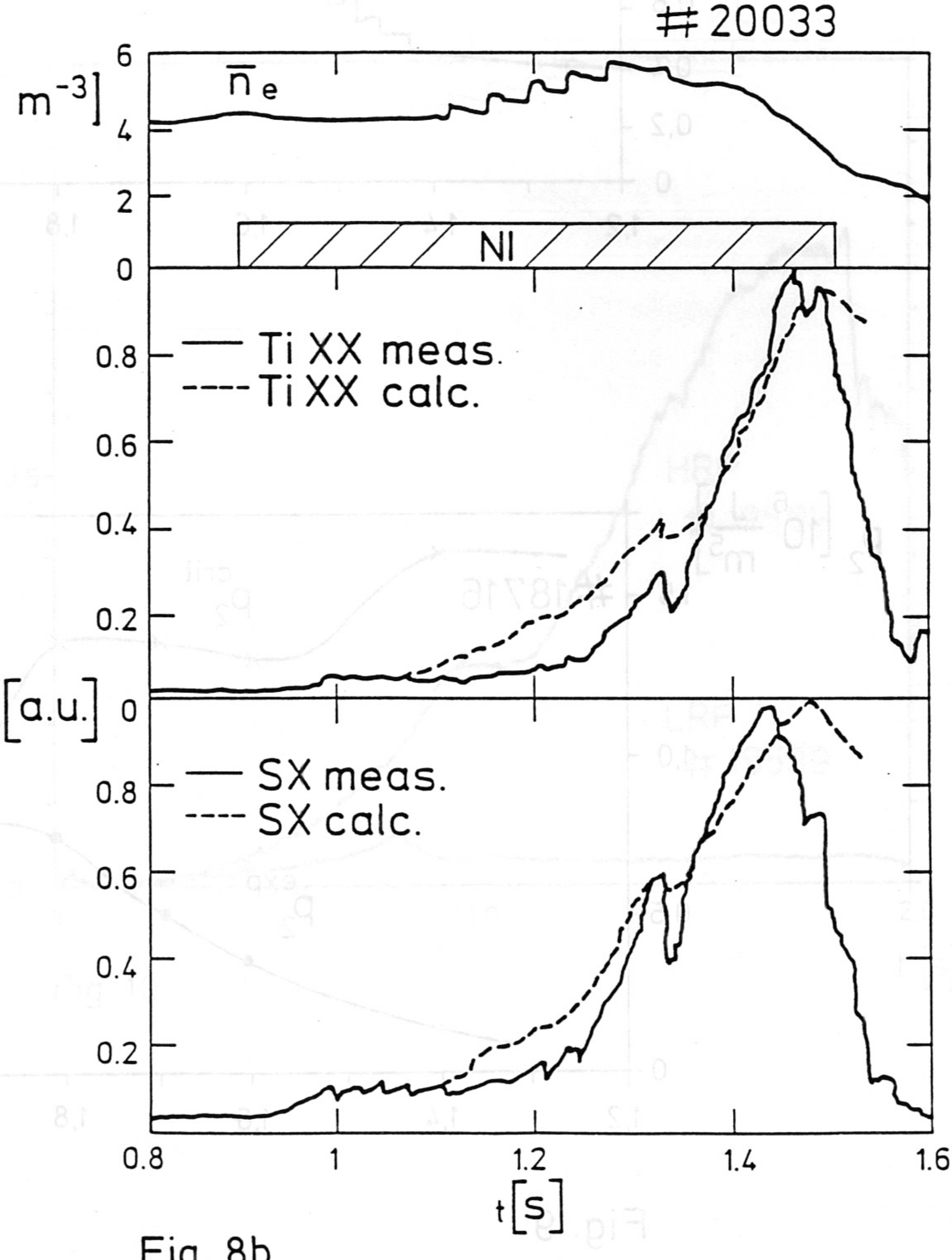

#20033
$\bar{n}_e$ [10^{19} m^{-3}]
$\bar{n}_e$
6
4
2
0
NI
Ti XX meas.
Ti XX calc.
0.8
0.6
0.4
0.2
0
[a.u.]
SX meas.
SX calc.
0.8
0.6
0.4
0.2
0.8
1
1.2
1.4
1.6
t[s]

Fig. 8b

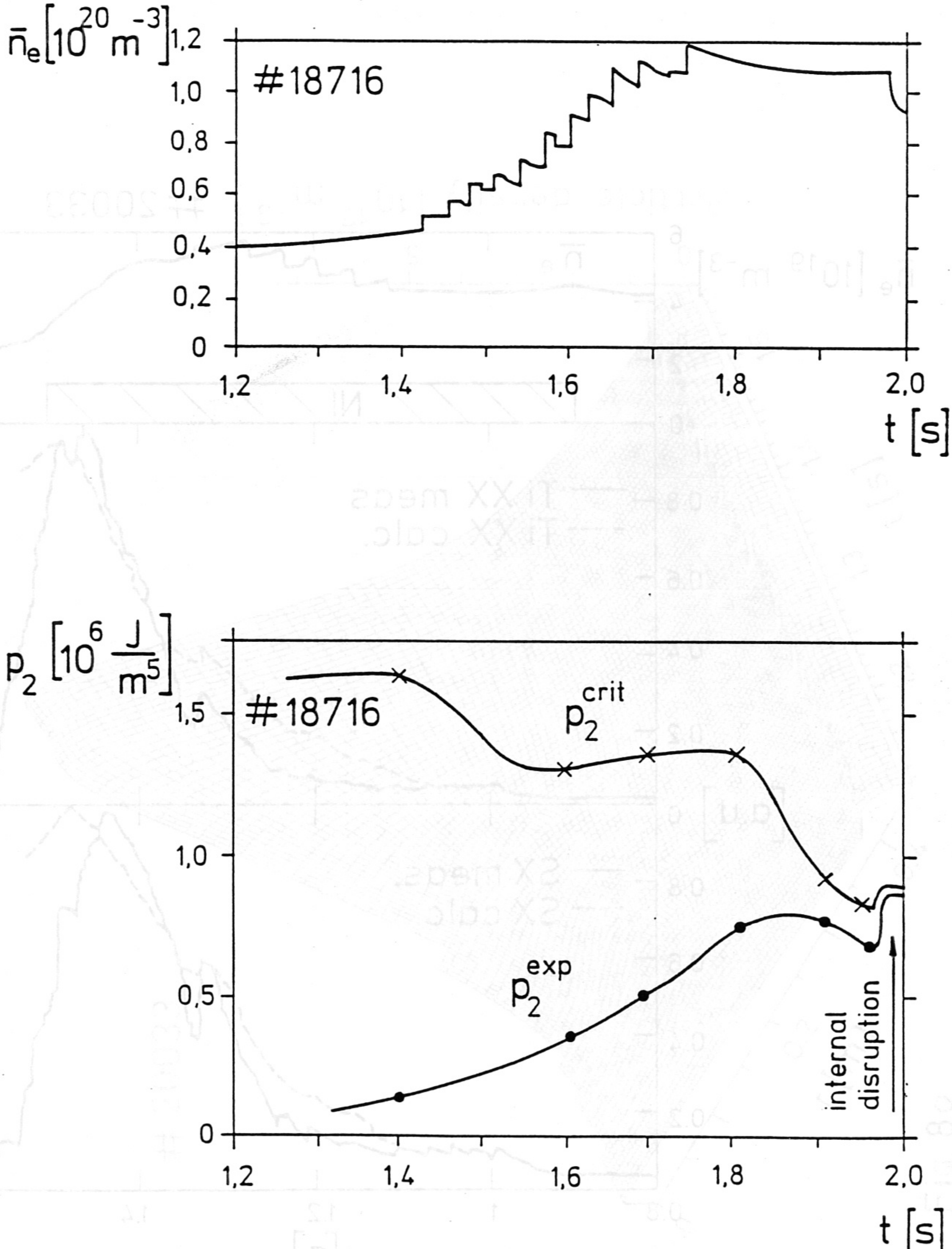

$\bar{n}_e\,[10^{20}\,m^{-3}]$
#18716
1,2
1,0
0,8
0,6
0,4
0,2
0
1,2
1,4
1,6
1,8
2,0
t [s]
$p_2\,[10^6\,\frac{J}{m^5}]$
#18716
p_2^{crit}
p_2^{exp}
1,5
1,0
0,5
0
internal disruption
1,2
1,4
1,6
1,8
2,0
t [s]

Fig. 9

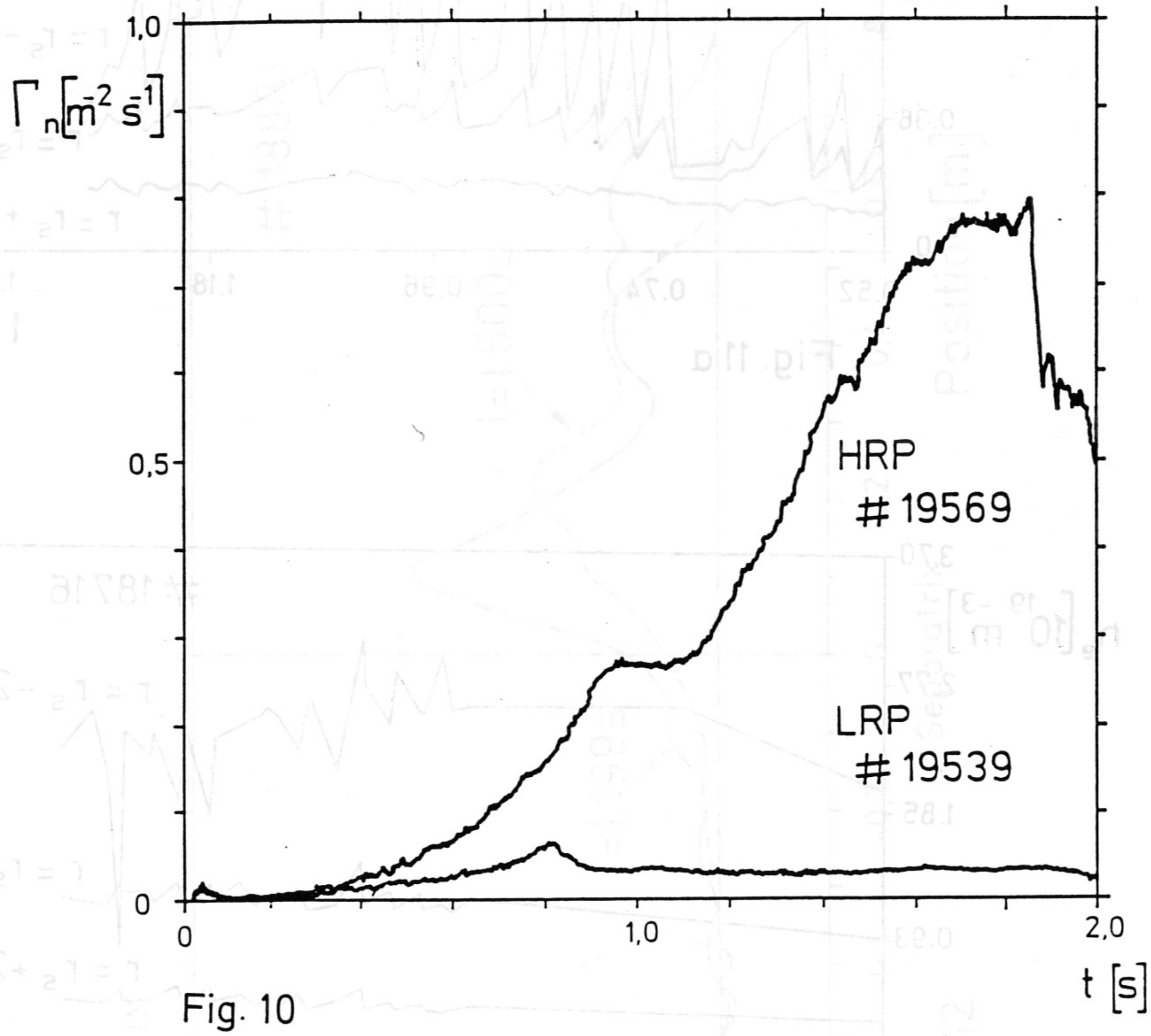

Fig. 10

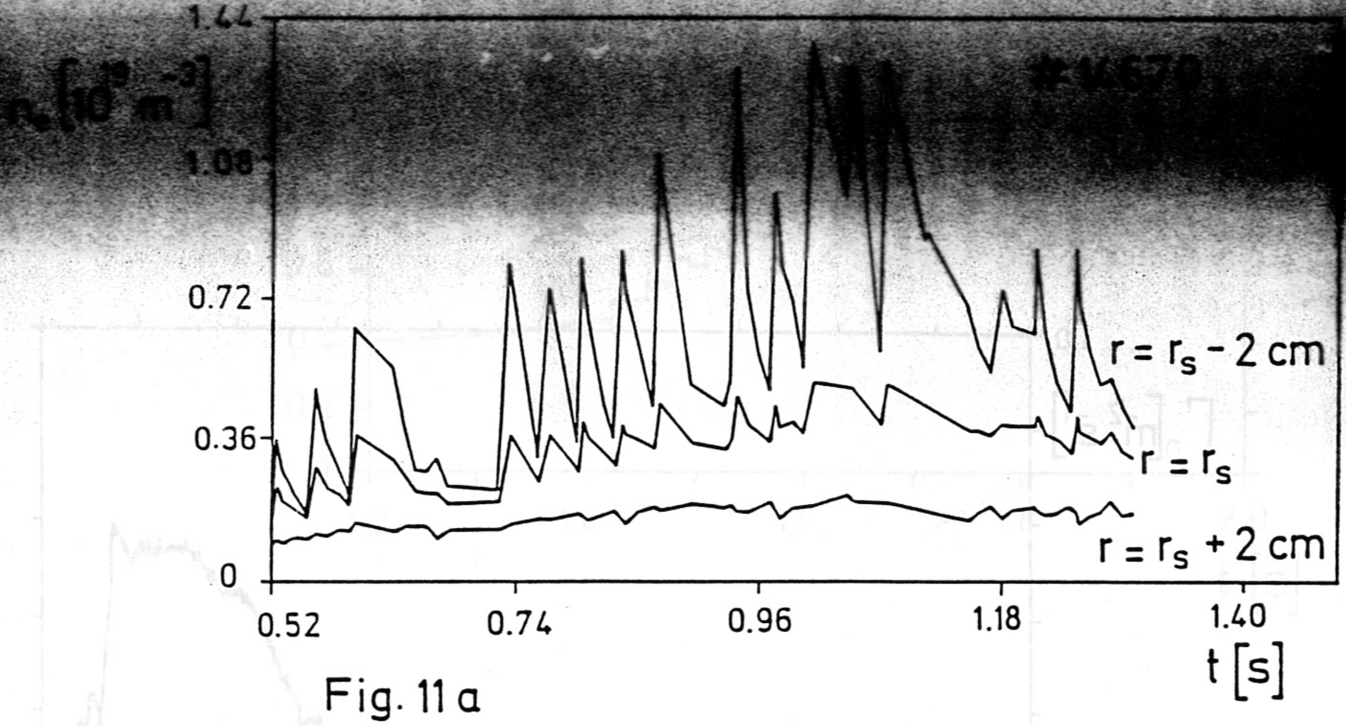

Fig. 11 a

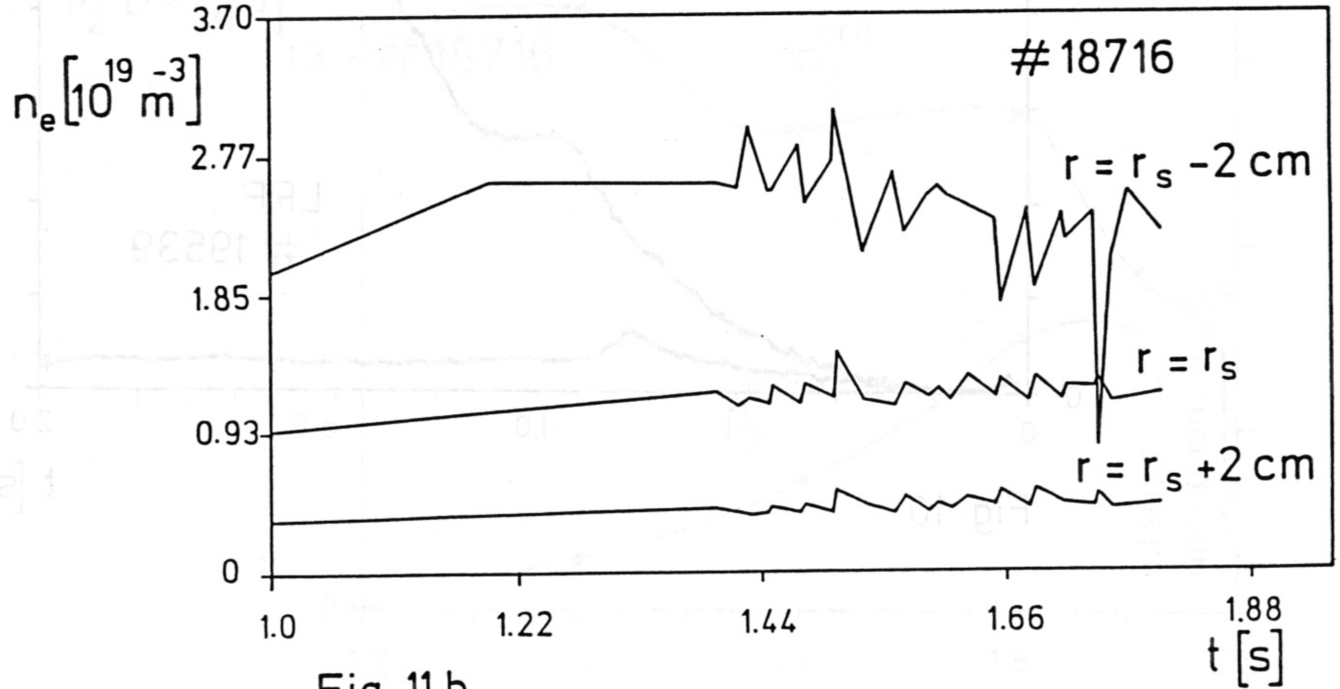

Fig. 11 b

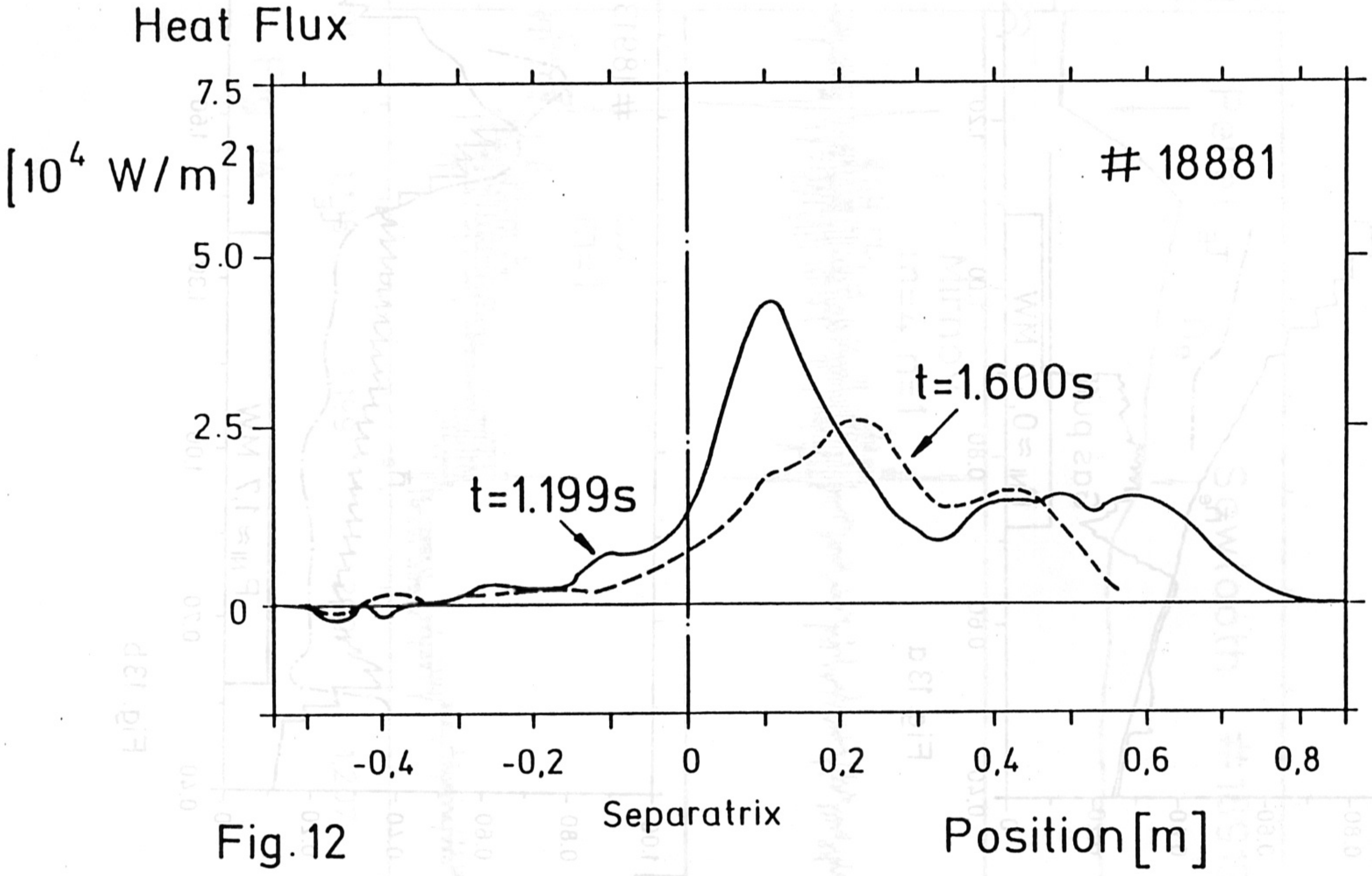
Heat Flux
[10^4 W/m^2]
7.5
5.0
2.5
0
# 18881
t=1.600s
t=1.199s
-0,4
-0,2
0
0,2
0,4
0,6
0,8
Separatrix
Position [m]

Fig. 12

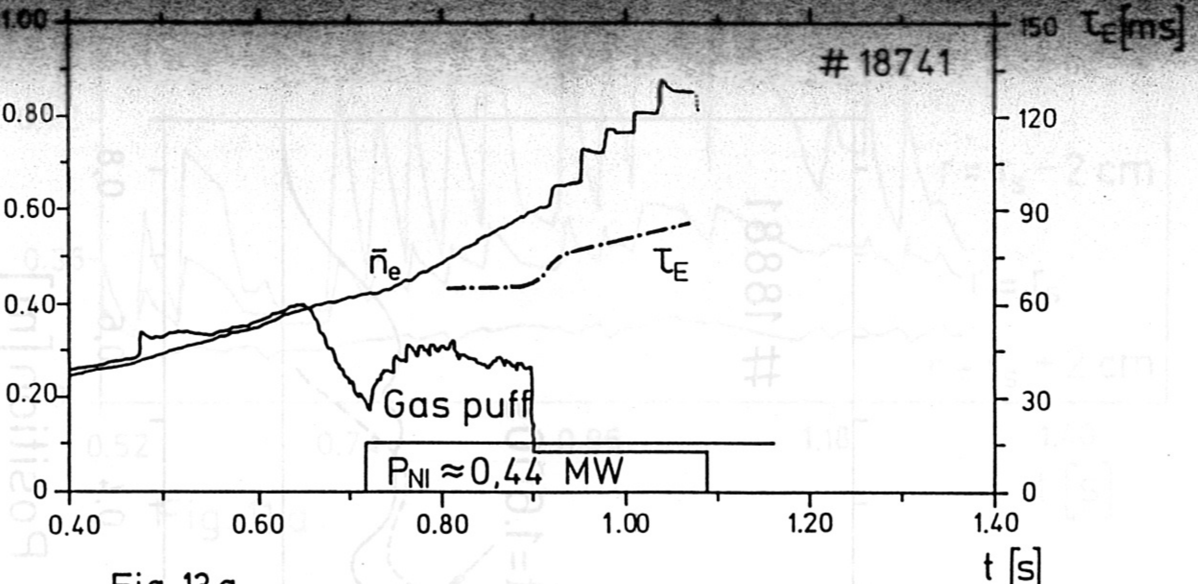

Fig. 13 a

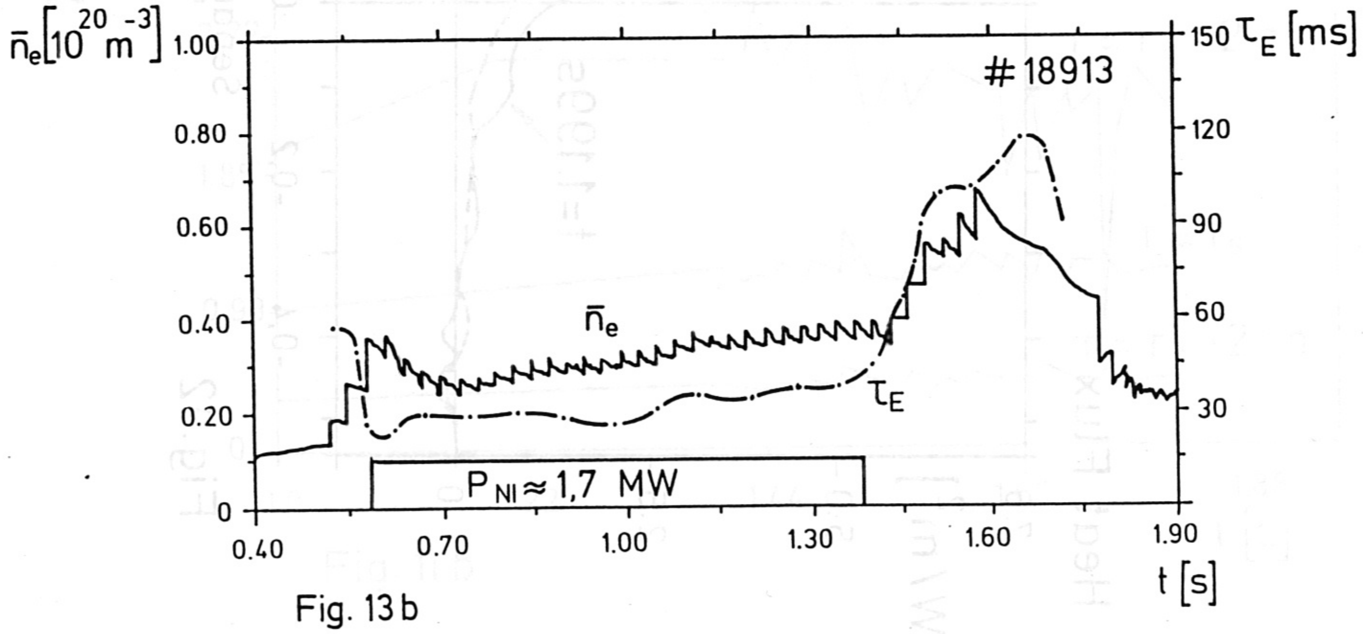

Fig. 13 b

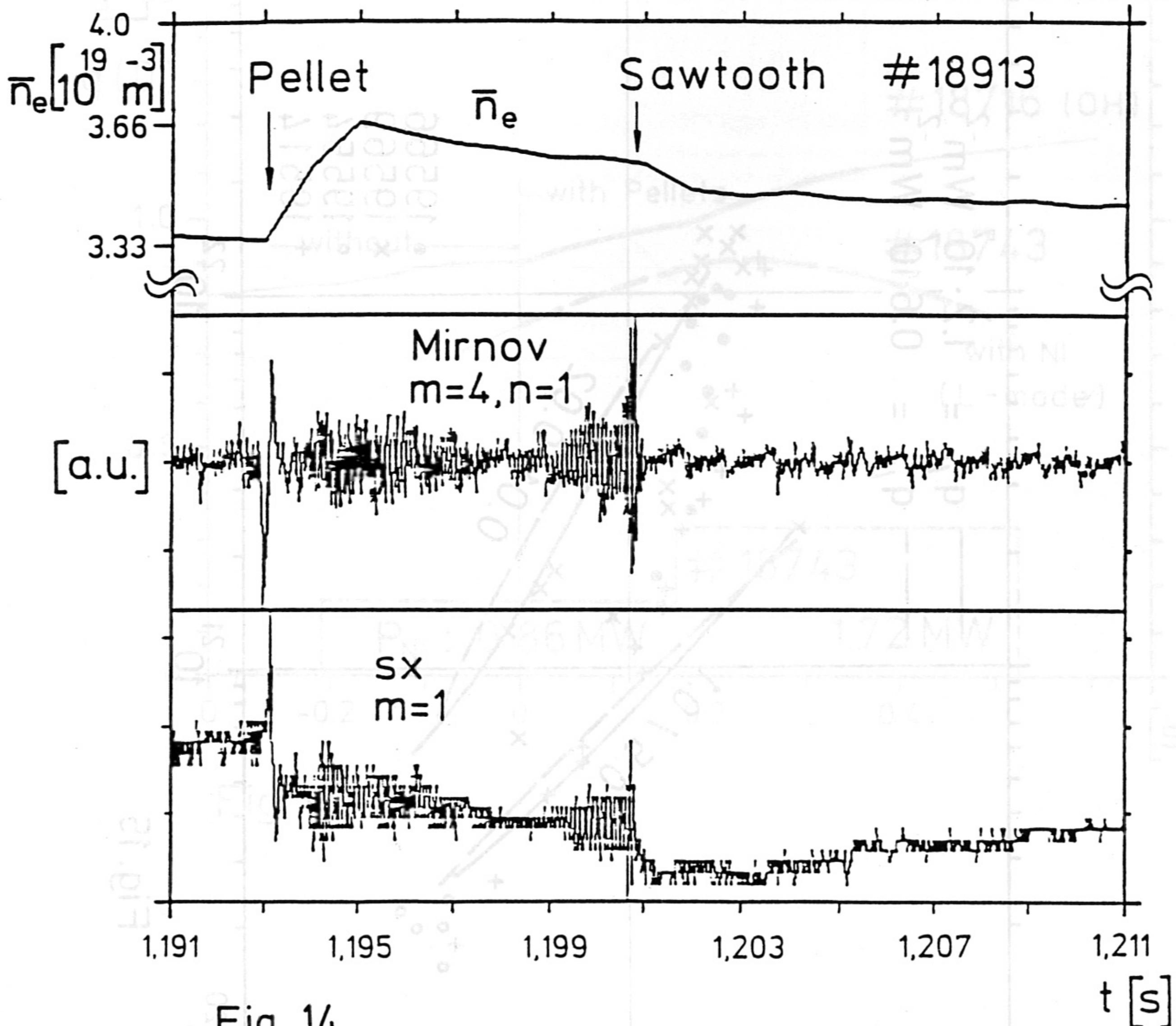
4.0
$\bar{n}_e[10^{19}\,m^{-3}]$
3.66
3.33
Pellet
$\bar{n}_e$
Sawtooth
#18913
Mirnov
m=4, n=1
[a.u.]
sx
m=1
1,191
1,195
1,199
1,203
1,207
1,211
t [s]

Fig. 14

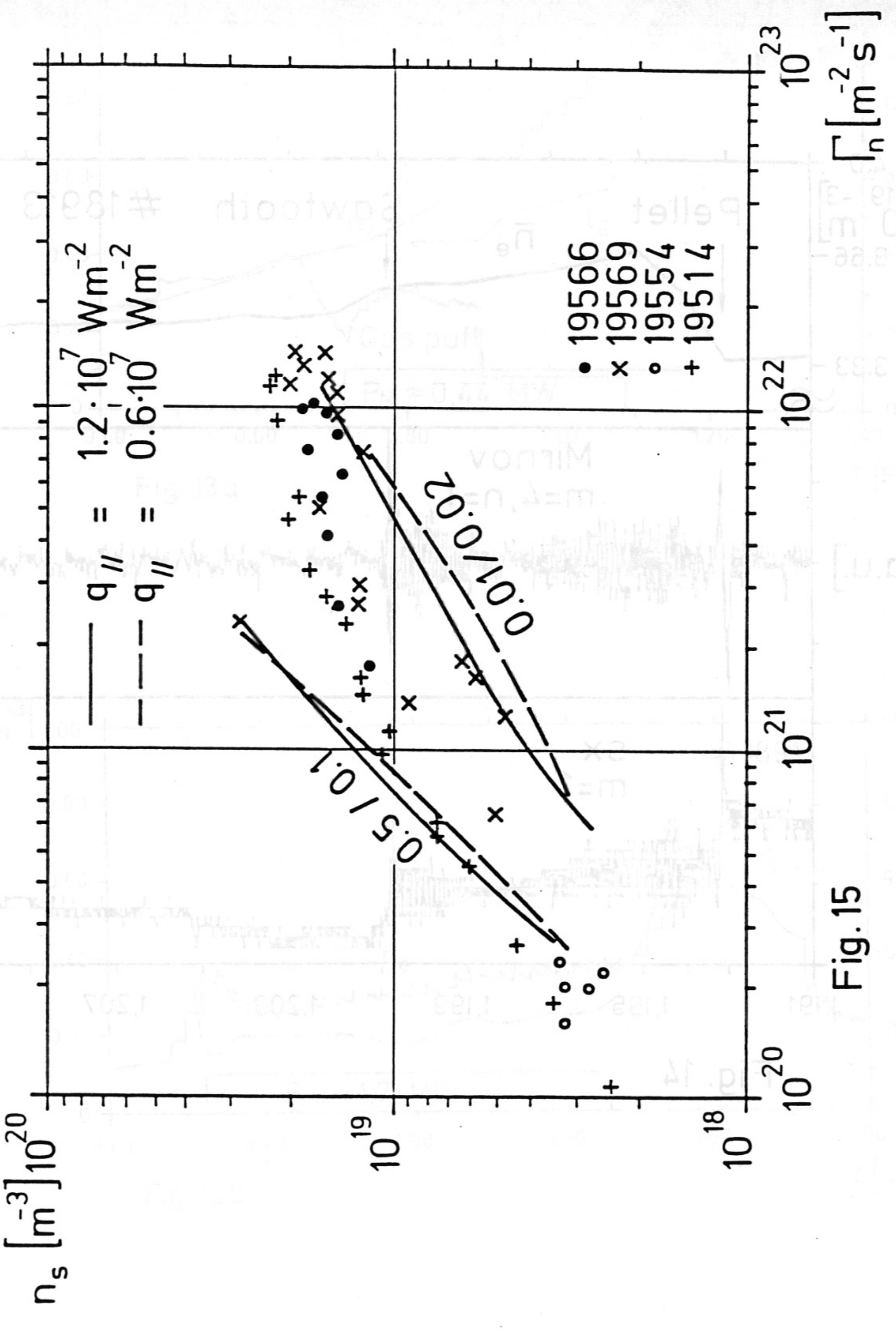
n_s [m^-3]
10^20
10^19
10^18
10^20
10^21
10^22
10^23
Γ_n [m^-2 s^-1]
q_// = 1.2·10^7 Wm^-2
q_// = 0.6·10^7 Wm^-2
0.5 / 0.1
0.01 / 0.02
● 19566
× 19569
∘ 19554
+ 19514

Fig.15

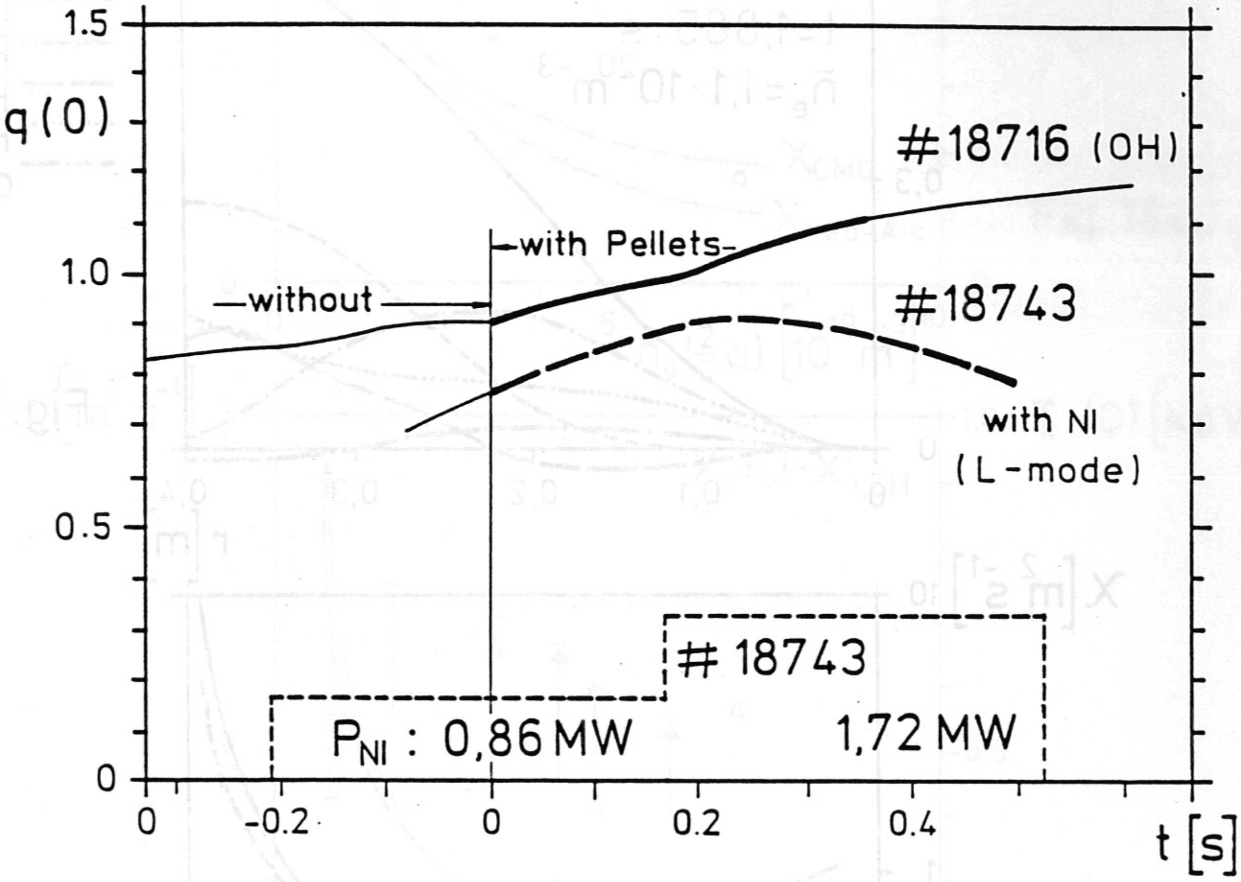

q(0)
1.5
1.0
0.5
0
#18716 (OH)
#18743
with NI
(L-mode)
—without
with Pellets
18743
P_NI : 0,86 MW
1,72 MW
0
-0.2
0
0.2
0.4
t [s]

Fig. 16

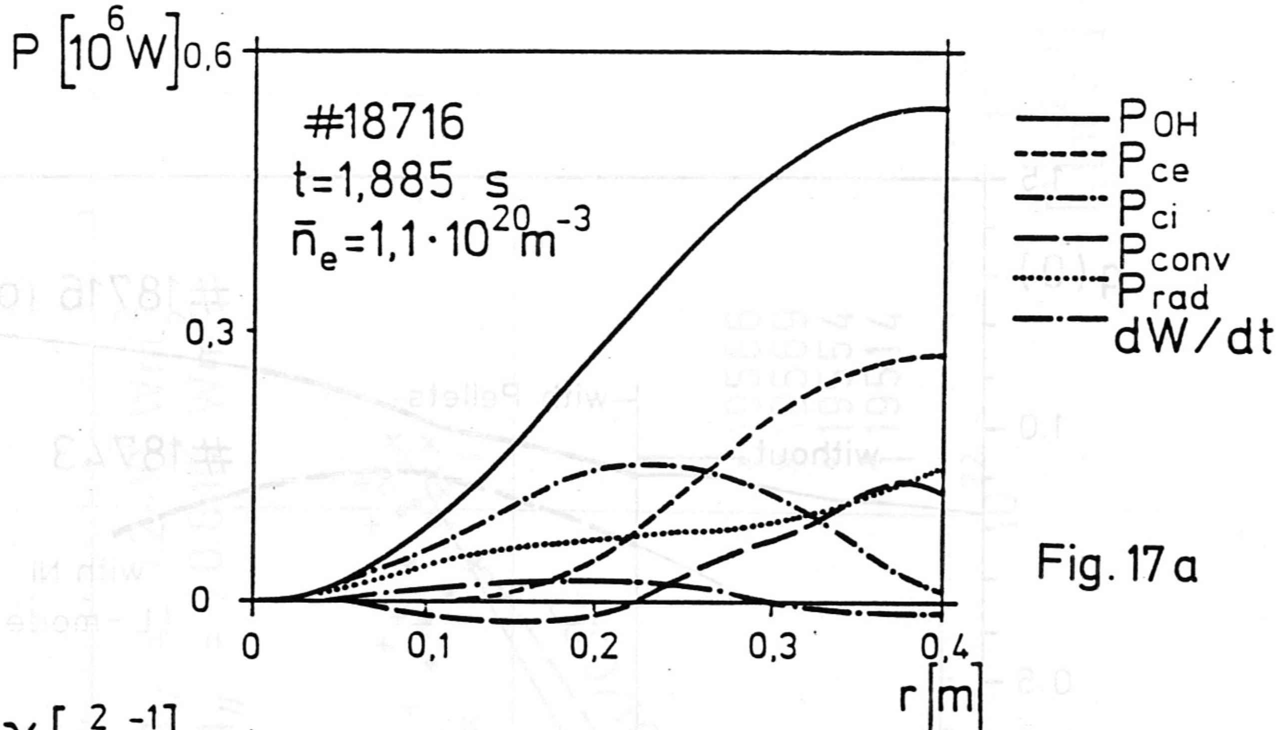

Fig. 17a

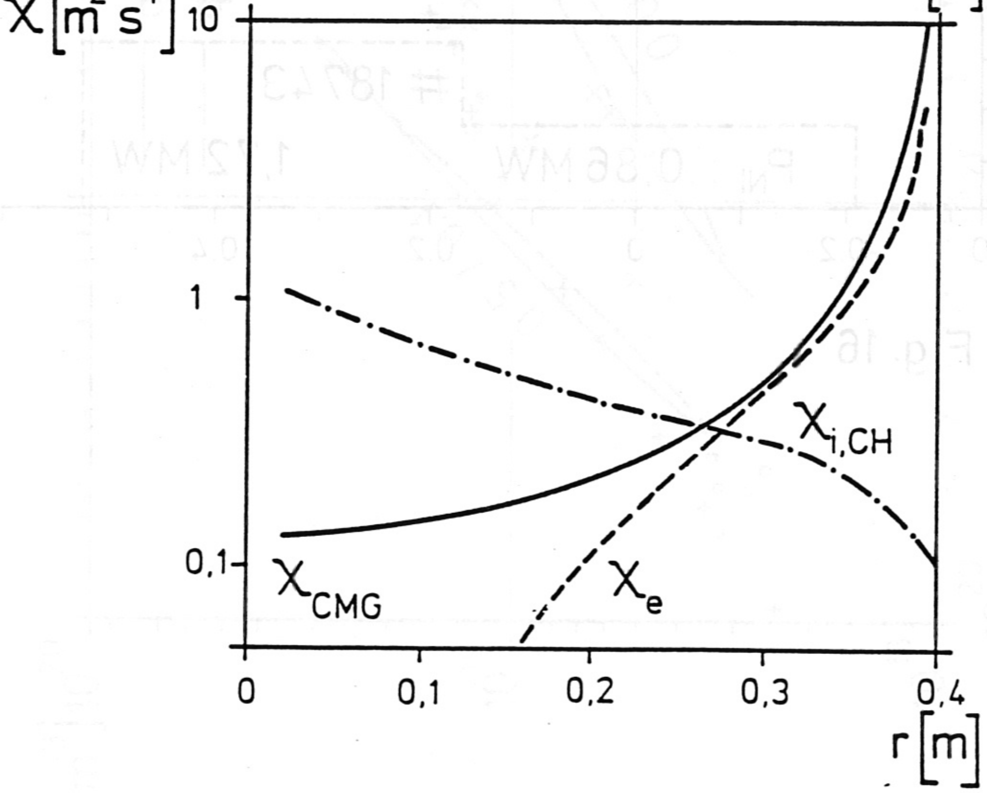

Fig. 17b

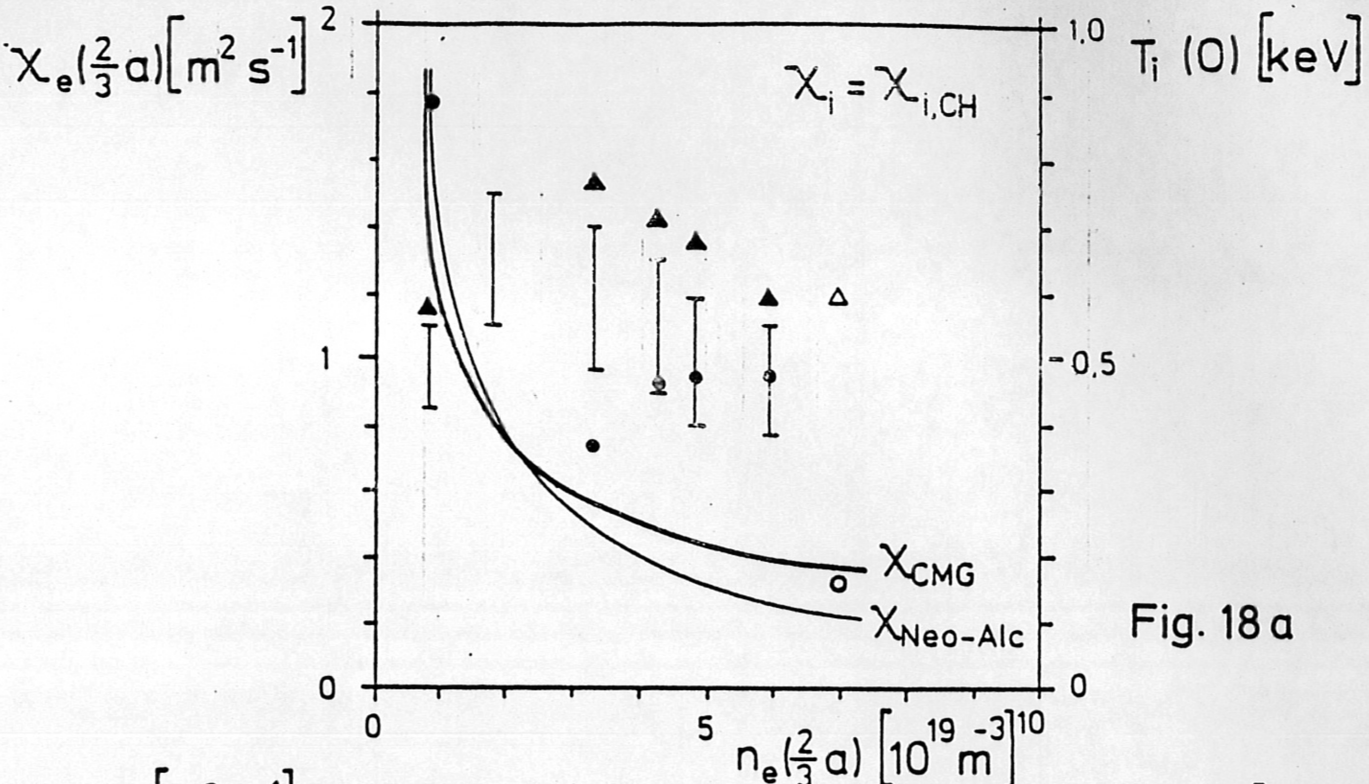

Fig. 18 a

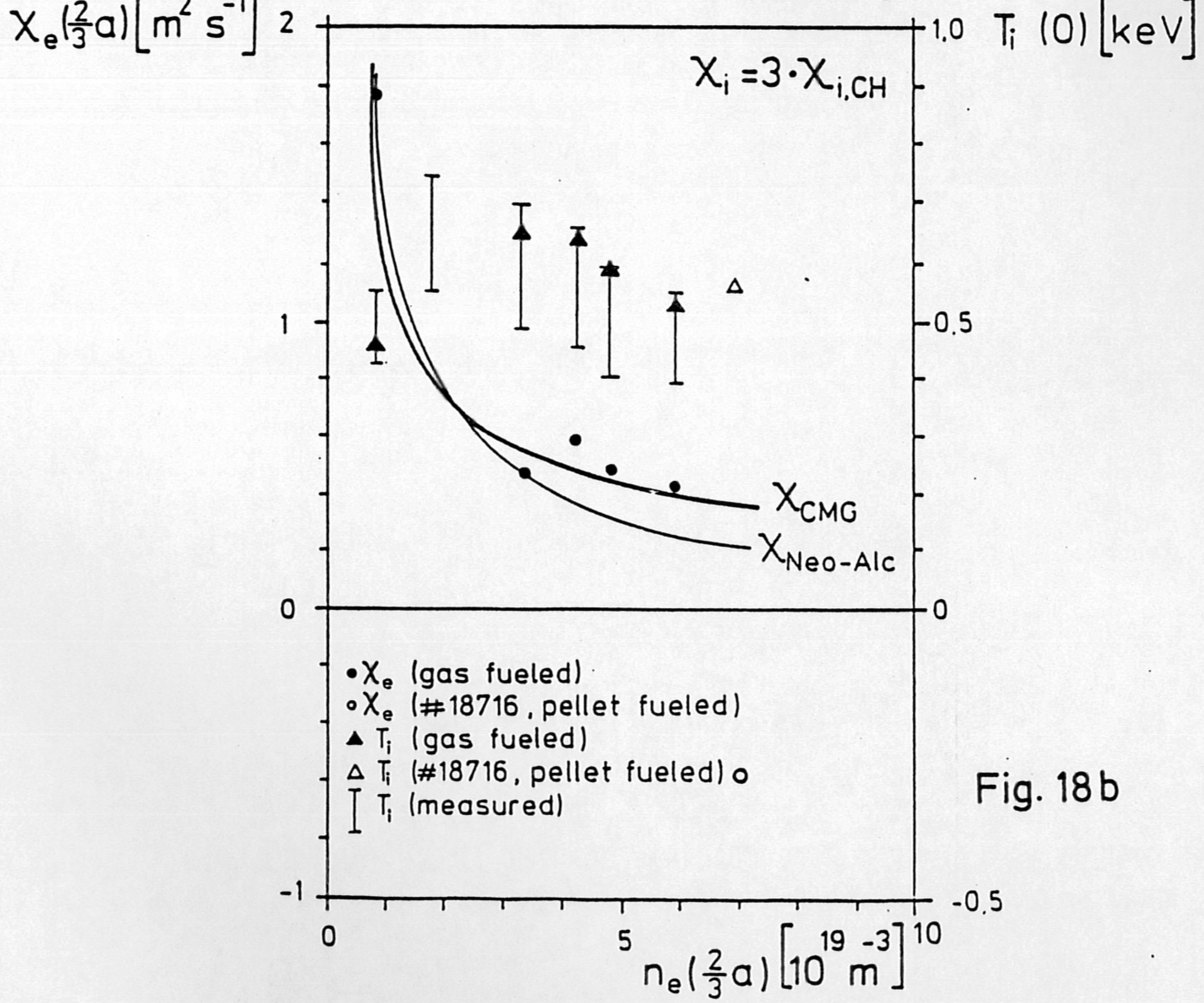

Fig. 18 b